Steel and Composite Structures, *Vol. 33, No. 2* (*2019*) *277-298*
DOI: https://doi.org/10.12989/scs.2019.33.2.277

Hysteresis modeling for cyclic behavior of concrete-steel composite joints using modified CSO

Yang Yu [1,3a], Bijan Samali [1b], Chunwei Zhang*[2b] and Mohsen Askari [1a]

[1] *Centre for Infrastructure Engineering*, *Western Sydney University*, *Penrith*, *NSW 2751*, *Australia*
[2] *School of Civil Engineering*, *Qingdao University of Technology*, *Qingdao*, *Shandong 266033*, *China*
[3] *School of Civil and Environmental Engineering*, *University of Technology Sydney*, *Ultimo*, *NSW 2007*, *Australia*

(*Received May 11, 2019, Revised August 15, 2019, Accepted October 14, 2019*)

Abstract. Concrete filled steel tubular (CFST) column joints with composite beams have been widely used as lateral loading resisting elements in civil infrastructure. To better utilize these innovative joints for the application of structural seismic design and analysis, it is of great importance to investigate the dynamic behavior of the joint under cyclic loading. With this aim in mind, a novel phenomenal model has been put forward in this paper, in which a Bouc-Wen hysteresis component is employed to portray the strength and stiffness deterioration phenomenon caused by increment of loading cycle. Then, a modified chicken swarm optimization algorithm was used to estimate the optimal model parameters via solving a global minimum optimization problem. Finally, the experimental data tested from five specimens subjected to cyclic loadings were used to validate the performance of the proposed model. The results effectively demonstrate that the proposed model is an easy and more realistic tool that can be used for the pre-design of CFST column joints with reduced beam section (RBS) composite beams.

Keywords: composite joint; cyclic loading; hysteresis; model identification; chicken swarm optimization

1. Introduction

Concrete filled steel tubular (CFST) column joints are being utilized in high-rise buildings and other structural systems due to advantages of high bearing capacity, earthquake-resistant property and easy construction (Han *et al*. 2019, Li *et al*. 2018a, Ma *et al.* 2019, Thai and Uy 2015). They effectively transfer loadings from the beams to columns, such as axial force, shear force, bending moment and torsional moment. Generally, the predominant factor for failure is the bending moment compared with other loads in moment-resisting frames (McCrum *et al*. 2019, Thai and Uy 2016, Wang *et al*. 2018). Accordingly, it is significantly important to investigate the nonlinear relationship between bending moment and rotation of the joint under lateral cyclic loading and to develop the phenomenological model to characterize the seismic performance of the joint.

When the structural members are subjected to the seismic/cyclic loading, the corresponding loading-deformation response becomes highly nonlinear with complicated hysteresis (Li *et al*. 2017a, 2018b, Wang *et al*. 2019). In the meantime, the stiffness and strength degradations are intrinsic damage phenomenon that exists in the hysteresis behaviour of the structural member. To date, there are a large number of hysteresis models proposed to incorporate the characteristics of strength and stiffness degradations, including elasto-plastic model (Veletsos *et al*. 1965), hysteretic shear model (Ozcebe and Saatcioglu 1989), bi-linear stiffness degradation model (Clough and Johnston 1966), energy-based hysteresis model (Ibarra *et al*. 2005), bi-axial hysteresis model (Chao and Loh 2009), enhanced smooth hysteresis model (Ray and Reinhorn 2014), degrading smooth model (Sofianos and Koumousis 2018, Wang *et al*. 2017), tri-linear stiffness degradation model (Otani and Sozen 1974), pivot hysteretic model (Dowell *et al*. 1998), neural networks-based model (Farrokh *et al.* 2015), Bouc-Wen-based hysteresis model (Baber and Noori 1985, Baber and Wen 1981, Wen 1976) and hysteresis model with the effect of shear and axial load failure (Sezen and Chowdhury 2009). Among these hysteresis models, the Bouc-Wen-based model is widely utilized in many engineering applications, because it is capable of portraying various hysteresis shapes of structural members and incorporating the characteristics of stiffness and strength deteriorations and pinching (Ning *et al*. 2016). The Bouc-Wen model was firstly designed by Bouc and then generalized by Wen, Baber and Noori (Baber and Noori 1985, Baber and Wen 1981, Wen 1976). Foliente developed a hysteresis model based on the modification of Bouc-Wen model for single and multiple degrees of freedom wood joints (Foliente 1995). The experimental results confirmed that this model is able to produce a smoothly changing hysteretic loop and capture the behaviours of nonlinear, inelastic, stiffness and strength degradations and pinching of the joints. Nithyadharan and Kalyanaraman employed the Bouc-Wen model to characterize the degrading phenomenon of the stiffness and strength with rigorous pinching for cold-formed steel shear

*Corresponding author, Professor,
E-mail: zhangchunwei@qut.edu.cn
[a] Ph.D.
[b] Professor

Copyright © 2019 Techno-Press, Ltd.

ISSN: 1229-9367 (Print), 1598-6233 (Online)

wall panel under cyclic loading (Nithyadharan and Kalyanaraman 2013). Sengupta and Li proposed an analytical model based on improved Bouc-Wen model to forecast the hysteretic response of reinforced concrete (RC) beam-column joints with limited transverse reinforcement and this model can portray the characteristics of non-seismic detailed beam-column joints such as strength and stiffness deteriorations and pinching (Sengupta and Li 2013). Similarly, they utilized this hysteretic model to depict the characteristics of requisite degradation and pinching of RC walls (Sengupta and Li 2014). Yu et al. adopted the Bouc-Wen model to predict the inelastic restoring force of shear-critical columns, and Newton-Raphson and backward Euler strategies were used to determine the value of the force via tackling the differential equations (Yu *et al*. 2016). Furthermore, the Bouc-Wen model has been employed to investigate inherent nonlinearities for the design and analysis of base-isolated steel buildings (Varnava and Komodromos 2013).

Although the Bouc-Wen model has been proved to be effective in characterizing the hysteresis with degradation and pinching phenomenon, it belongs to the numerical model family and the model parameters should be identified using the data collected from experimental tests. Nevertheless, because of a large number of model parameters and complicated nonlinear differential equation in model expression, the studies on parameter identification of the Bouc-Wen model for CFST column-to-beam joints are rarely reported. Evolutionary computation algorithms, such as genetic algorithm (GA), can be used to identify such complex models. However, because the gradient information of the model formula cannot be directly expressed using explicit equation, it is unrealistic to identify the model parameters using commonly used gradient-based algorithms. Although the trust-region algorithm and simulated annealing method are capable of solving such a problem, the identification accuracy is dependent on the initial values of parameters to be identified, and the final solution may fall into the local optimum if the initial values are poorly selected.

A novel bio-inspired meta-heuristic algorithm, chicken swarm optimization (CSO), has been proposed recently as a new branch of swarm intelligence (Meng *et al*. 2014). This new optimization algorithm is based on the imitation of hierarchy and food search behaviour of the chicken. In CSO, the swarm is usually divided into cocks, hens and chicks. The cocks are the chickens with the highest fitness values while the chicks are the chickens with the lowest fitness values. Except the cocks and chicks, the rest of the chickens are regarded as the hens. When the CSO is employed to deal with optimization problems, each chicken is a possible solution and different search methods are utilized for different chicken categories. Compared with other homogeneous swarm-based algorithms such as particle swarm optimization (PSO) and fruit fly algorithm (FFA), the CSO has better performances in both convergence rate and searching accuracy, and thus has been widely utilized in various engineering fields, such as wireless sensor networks localization (Al Shayokh and Shin 2017), water quality evaluation (Liu *et al*. 2018) and nonlinear system identification (Chen *et al*. 2016). The searching strategy and parameter setting of the CSO can be found in (Meng *et al*. 2014, Wu *et al*. 2016), where the problem on algorithm convergence rate is also discussed.

In this study, the Bouc-Wen model is firstly applied in characterizing the nonlinear bending moment-rotation responses of CFST column-to-composite beam joints under cyclic loading and a novel rotational hysteresis model is proposed accordingly, which incorporates damage-related factors to indicate strength degradation and stiffness deterioration induced by the increment of loading displacement and cycle number. Then, the CSO algorithm is employed to identify the parameters of the proposed rotational hysteresis model. The model identification procedure can be regarded as solving a global minimization optimization problem, in which the optimization object is the root mean square (RMS) error between experimental results and model outputs. To enhance the solution accuracy and algorithm convergence, the CSO is modified by improving the search ability of the chicks in the swarm, the performance of which is verified via the comparison with original CSO and other algorithms. Finally, based on bending moment-rotation data tested from five composite cruciform joints, the parameters of the proposed rotational hysteresis model are identified using the modified CSO (M-CSO). The results demonstrate that the proposed model can not only capture the cyclic responses of the composite joints, but is also able to accurately predict the structural strength degradation, stiffness deterioration and energy dissipation.

2. Experimental program

2.1 Specimen design

In this study, five composite cruciform joint specimens are designed and constructed in accordance with the provisions of AS 2327.1 (2003), EC 3 (2005) and EC 4 (2006). Among five specimens, the specimen S-1 is designed as the reference without any slab or beam cut, while RC slabs and RBS beams are employed for the remaining specimens, i.e., S-2, S-3, S-4 and S-5. Fig. 1 illustrates the design information of the specimens S-2, S-3, S-4 and S-5, in which different cut depths and lengths are considered for the beam design. Expect no slab and beam cut, the S-1 has the same design as other four specimens. The detailed information of five joint specimens are given in Table 1, where 'o' denotes the circular section, n denotes the axial loading level, k_m denotes the ratio of the column flexural capacity to the beam flexural capacity considering the effect of RC slab, k'_m denotes the ratio of the column flexural capacity to the beam flexural capacity without the effect of RC slab, $k_{m,RBS}$ denotes the ratio of the column flexural capacity to the beam flexural capacity considering the effect of RBS, k_E denote the ratio of the column flexural stiffness to the beam flexural stiffness considering the effect of RC slab, k'_E denotes the ratio of the column flexural stiffness to the beam flexural stiffness without the effect of RC slab, $k_{E,RBS}$ denotes the ratio of the column flexural

stiffness to the beam flexural stiffness considering the effect of RBS, h_b denotes the depth of the beam, b_f denotes the width of the beam flange, t_w denotes the thickness of the beam web and t_f denotes the thickness of the beam flange.

It can be observed from Fig. 1 that the composite joint is designed half the full-scale. The cylindrical steel tube is designed with the diameter of 250 mm and wall thickness of 6 mm. The beam is designed to be 1500 mm long from

Table 1 Details of composite joint specimens

No.	Column $D\times t_s$	Beam $h_b\times b_f\times t_w\times t_f$ (mm)	Cut depth of RBS (mm)	n	k_m	k'_m	$k_{m,RBS}$	k_E	k'_E	$k_{E,RBS}$	Slab
S-1	o-250×6	248×124×5×8	0	0.4	–	1.81	–	–	1.26	–	No
S-2	o-250×6	203×133×5.8×7.8	26 (0.2b_f)	0.4	1.22	–	1.38	1.47	–	1.67	Yes
S-3	o-250×6	203×133×5.8×7.8	34 (0.25b_f)	0.4	1.22	–	1.41	1.47	–	1.73	Yes
S-4	o-250×6	248×124×5×8	25 (0.2b_f)	0.4	1.03	–	1.16	1.06	–	1.20	Yes
S-5	o-250×6	248×124×5×8	31 (0.25b_f)	0.4	1.03	–	1.19	1.06	–	1.24	Yes

Table 2 Steel element material properties

Parameter	Steel element					
	Shear stud	Reinforcement	UB web	UB flange	Steel tube	Through diaphragm
σ_f (MPa)	487.5	639.6	468.9	455.6	480.4	440.7
σ_y (MPa)	402.3	609.7	344.6	299.9	386.6	289.7
ε_y ($\mu\varepsilon$)	1,841	3,197	1,537	1,418	2,315	3,217
E_m (MPa)	200,713	203,238	204,120	201,516	199,433	201,745
t or d (mm)	Φ12	Φ10	8.6	14.2	6.0	10.1
δ	34.1	24.5	34.3	37.6	27.9	38.3

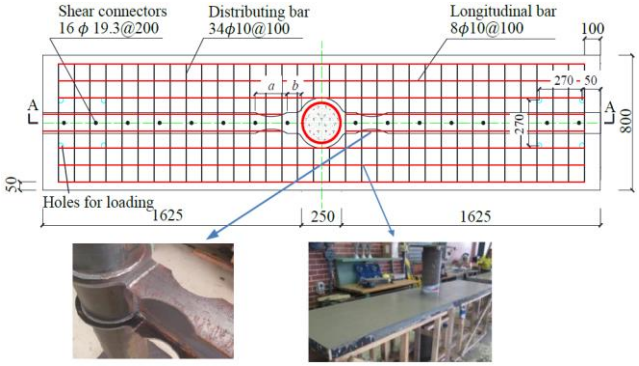

(a) Top view

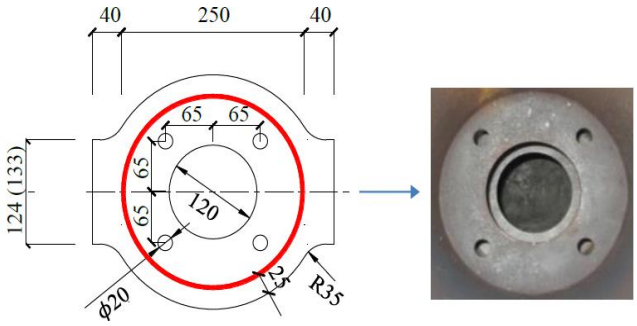

(b) Through diaphragm

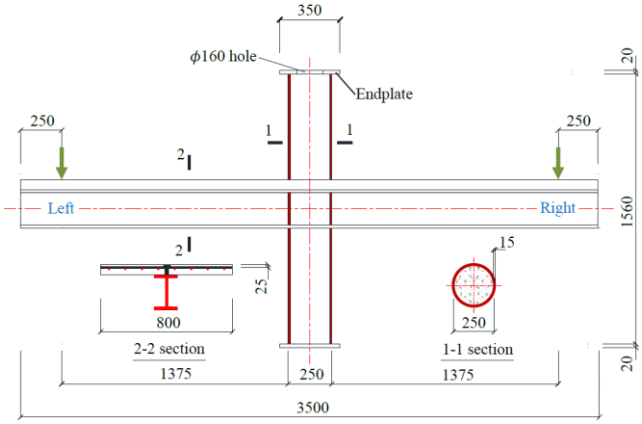

(c) Elevation

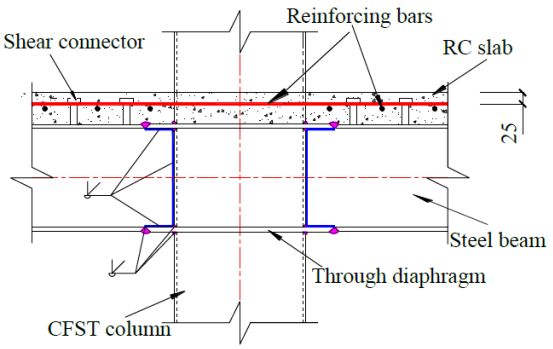

(d) A-A section (refer to (a))

Fig. 1 Specimen configuration

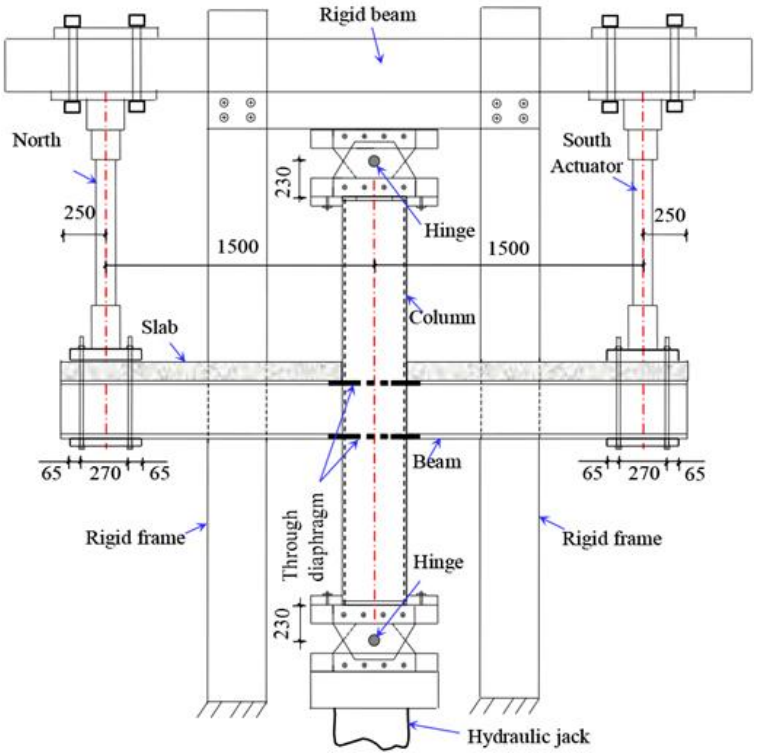

Fig. 2 Schematic of experimental setup

column center to beam inflection point. The depth and width of the RC slab is designed to be 60 mm and 800 mm. To connect the beam to the column, the through diagrams with the thickness of 10 mm are employed in this design, the inner diameter, out diameter and diameter of vent hole of which are 120 mm, 300 mm and 20 mm. 42 pieces of rebar with the diameter of 10 mm, including 8 longitudinal bars and 34 distributing bars, are put in the slab, which are transversely and longitudinally distributed along the slab with the space of 100 mm. The CFST columns are same for five composite joint specimens. The detail description about specimen design can also be found in (Li *et al.* 2017b).

2.2 Properties of materials

The grade of concrete is C32, i.e., compressive strength of 32 MPa. The tests for the material properties of concrete are conducted in accordance with AS 1012.9 (2014) and AS 1012.10 (2014). The corresponding results are given as follows: the tensile strength and compressive strength of the cylinder specimen are 4.7 MPa and 36.5 MPa, respectively; the elastic modulus is 37,740 MPa. For the steel material, the material properties are evaluated using tensile coupon tests, and six steel elements are considered including steel tube, UB web, UB flange, through diaphragm, steel reinforcement and shear stud. Table 2 lists the testing results of steel material properties, in which σ_f represents the ultimate strength, σ_y represents the yielding stress, ε_y represents the yielding point strain, E_m represents the elastic modulus, t is steel element thickens, d is the diameter of the steel reinforcement or shear stud, and δ represents the elongation factor.

2.3 Experimental setup and loading scheme

The experimental setup is described in Fig. 2, in which the quasi-static cyclic loading is applied to five specimens via a hydraulic jack, with the constant axial compressive load of 1,116 kN. Two hinges are installed at both bottom and top ends of the column, so the column is able to freely rotate in plane. The distances between the ends and their closest hinge centres are 230 mm. Two actuators, with the loading capacity of 500 kN, are connected with both ends of the beam to provide the cyclic loading. The distances between two loading points and the centre of the column are 1.5 m. Two actuators are set to provide the excitations with the same amplitudes but in opposite directions, simultaneously. The loading protocol of cyclic excitation amplitude is shown in Fig. 3. It can be seen from the figure that the loading is controlled by the inter-storey drift angle defined as inter-storey displacement divided by storey height. In this experimental study, this angle is defined as the ratio of beam deflection to beam span.

The whole loading history can be separated into different stages and the peak rotation of each loading level is a predefined value of the inter-storey drift angle. The beam deflection is to be used to control the rotation history, and the corresponding predefined rotations are given in Table 3. It can be seen from the table that the first three loading levels begin with six cycles at each loading level of 0.004 rad, 0.0053 rad and 0.0073 rad rotations, respectively. The next four cycles at 4th load step are at 0.01 rad rotation, followed by two cycles in 5th load step of 0.015 rad rotation. Then, the loading peak is gradually increased from 0.02 rad with the increment of 0.01 rad rotation and two

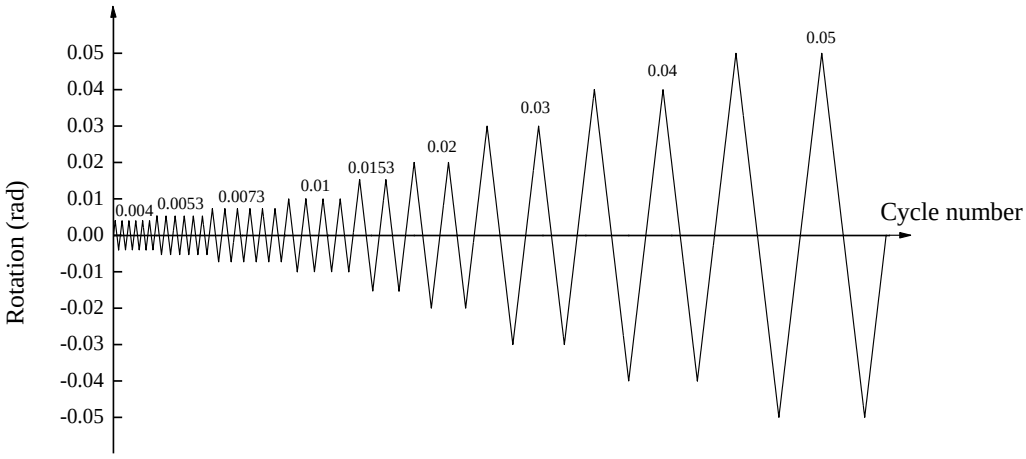

Fig. 3 Loading history

Table 3 Loading protocol

Loading level	Rotation (rad)	Cycle number of each loading level	Corresponding displacement (mm)
1	0.004	6	6
2	0.0053	6	8
3	0.0073	6	11
4	0.01	4	15
5	0.0153	2	23
6	0.02	2	30
7	0.03	2	45
8	0.04	2	60
9	0.05	2	75
10	0.06	2	90

* Continue with the increment of 0.01 rad and perform two cycles ateach level

cycles at each rotation level until the failure of the connection. The loading velocities of the actuators are controlled at 8 mm/min.

Different types of sensors are utilized to quantify the horizontal and vertical displacements of columns and beams of the joints, the deployment schematic of which is shown in Fig. 4. It can be seen from the figure that two LVDTs installed on the surface of the column in the horizontal direction are used to measure the displacement of the column, which can be used to calculate the rotation of the column. Four LVDTs deployed on the surface of the beam in the vertical direction together with four inclinometers are employed to measure the displacement of the beam, which can be used to calculate the rotation of the beam. In addition, the linear potentiometers are installed at two ends of the beam to estimate the interface slip between steel beam and RC slab.

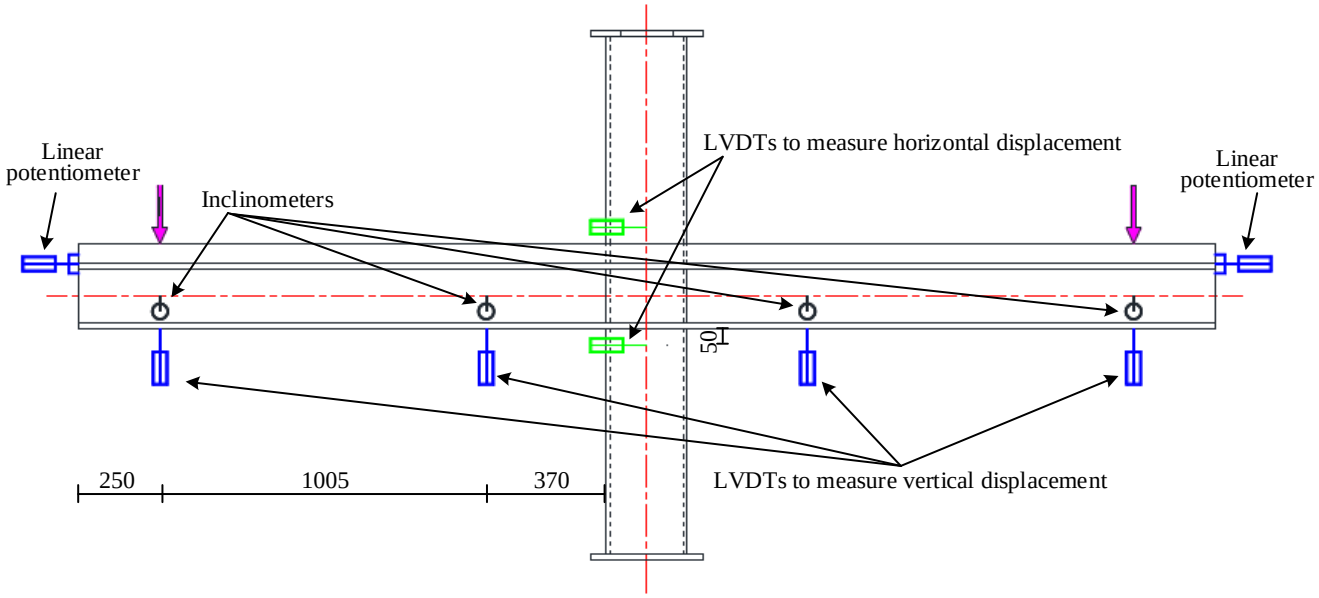

Fig. 4 Sensor deployment

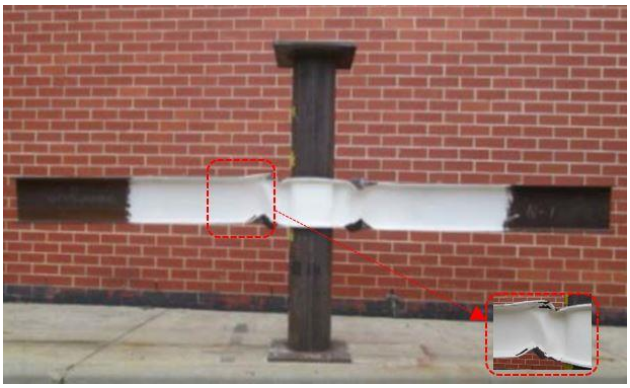

(a) Photo of final appearance

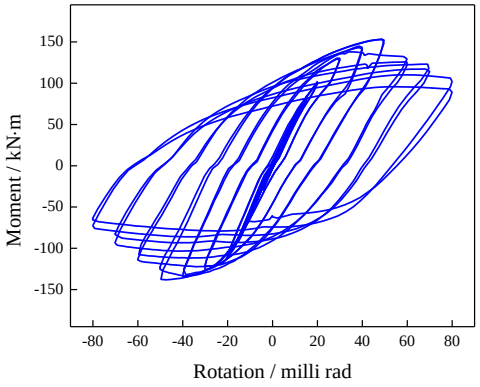

(b) Moment-rotation hysteresis loop

Fig. 5 Testing results of specimen S-1

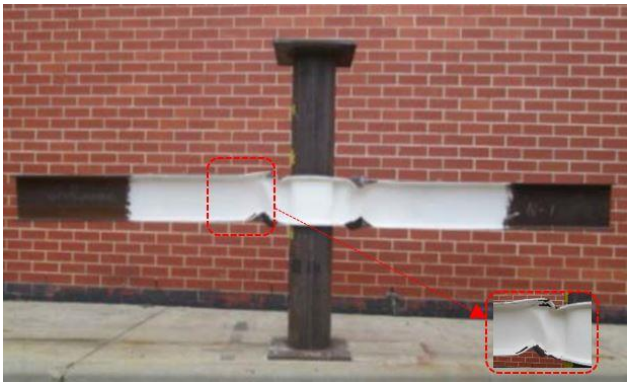

(a) Photo of final appearance

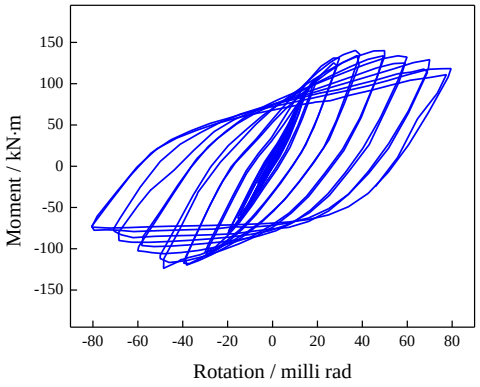

(b) Moment-rotation hysteresis loop

Fig. 6 Testing results of specimen S-2

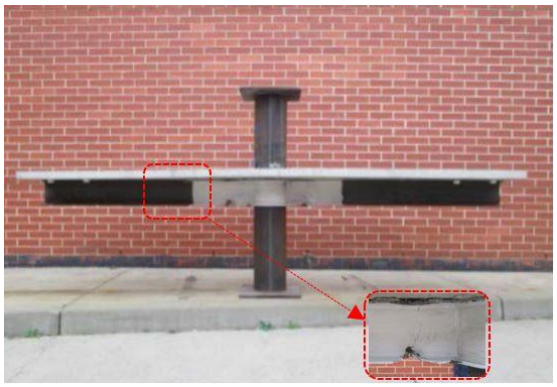

(a) Photo of final appearance

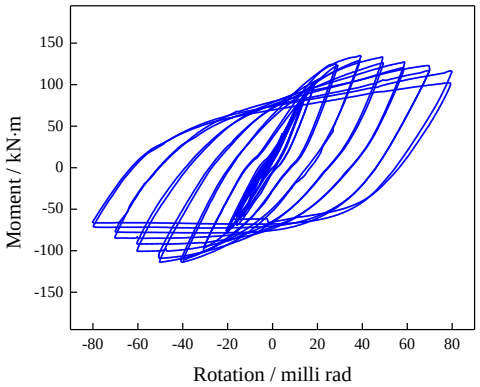

(b) Moment-rotation hysteresis loop

Fig. 7 Testing results of specimen S-3

2.4 Experimental results

The testing results of five joint specimens are shown in Figs. 5-9. The left figures (a) show the photos of ultimate joints' appearances, indicating that the failure modes of all specimens are beam failure. The right figures (b) provide nonlinear relationships between joint moments and rotations, which are of great significance to portray the capacity of the composite joints. Here, the joint moment is defined as the product of the beam span and loading applied at the tip of the beam, while the joint rotation is defined as the difference between the beam rotation and column rotation. It can be observed from the figures that all joints have exhibited good deformation performances and the corresponding hysteresis loops are chubby. Because of the existence of RC slabs, the hogging flexural resistance is lower than the sagging flexural resistance, which is capable of effectively improving the strength deterioration.

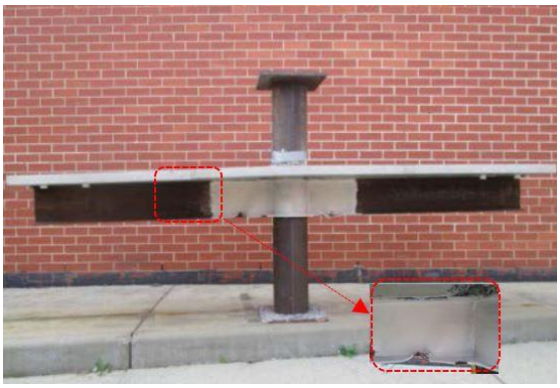

(a) Photo of final appearance

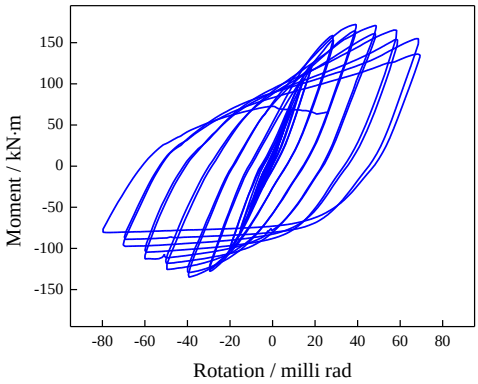

(b) Moment-rotation hysteresis loop

Fig. 8 Testing results of specimen S-4

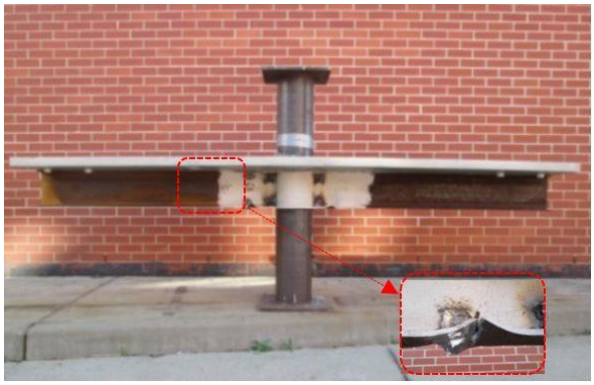

(a) Photo of final appearance

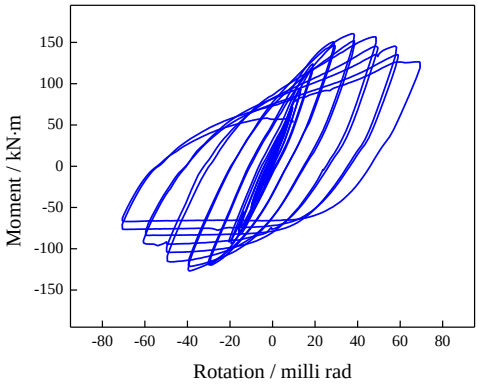

(b) Moment-rotation hysteresis loop

Fig. 9 Testing results of specimen S-5

However, the strength deterioration under hogging moment is little evident due to quick local yielding of bottom beam flanges.

3. Hysteresis modelling of composite joints under cyclic loading

Different from traditional finite element modelling, a novel phenomenological model is developed in this study, which is based on the curve fitting technology. According to the experimental phenomena and results of the joints in Section 2, the Bouc-Wen component with strength and stiffness degradation characteristics is employed to build up the model for characterizing the cyclic behaviour of the composite joints. The experimental data is then used to identify the model parameters via fitting the model predictions into the experimental hysteresis curve as close as possible. The details on model design and parameter identification will be given in the following subsections.

3.1 Description of the proposed rotational hysteresis model

In this part, a novel analytical model, based on the Bouc-Wen hysteresis model, is proposed to portray the nonlinear bending moment-rotation relationship of cyclic responses of the composite joints. Suppose the rotation movement of a single degree-of-freedom system is given by the following equation

$$T(\theta,\dot{\theta},y) = \alpha \cdot k_0 \cdot \theta + c_0 \cdot \dot{\theta} + (1-\alpha) \cdot k_0 \cdot y + T_0 \quad (1)$$

where T denotes the bending moment; α denotes the ratio of post-yield stiffness to initial stiffness; k_0 denotes the initial rotational stiffness factor; c_0 denotes the rotational damping factor; θ and $\dot{\theta}$ denote angular displacement and angular velocity, respectively; T_0 is the initial moment, which denotes the offset in this study; y is an intermediate variable and its value can be obtained from the following equation

$$\dot{y} = h(y) \cdot \frac{A \cdot \dot{\theta} - v \cdot (\beta \cdot |\dot{\theta}| \cdot |y|^{n-1} \cdot y + \gamma \cdot \dot{\theta} \cdot |y|^{n})}{\eta} \quad (2)$$

where A denotes the tangent stiffness; β, γ and n are parameters to regulate the hysteresis shape; v and η are parameters to designate strength and stiffness degradations, respectively; $h(y)$ is a function for the pinching phenomenon.

For the system without degradation and pinching, the continuous function can be used to designate the hysteresis phenomenon and hysteresis stiffness is 0 at local optimum

(minimum or maximum), where the sign of the velocity is changed. Consequently, at an infinitely small range *dy* away from y_{max}, where the velocity approximates to 0 and $\dot{y}_{max} \approx \dot{y}_1$

$$\dot{y}_{max} \approx A \cdot \dot{\theta} - v \cdot \begin{pmatrix} \beta \cdot |\dot{\theta}| \cdot |y|^{n-1} \cdot y \\ +\gamma \cdot \dot{\theta} \cdot |y|^n \end{pmatrix} = 0 \quad (3)$$

$$y_{max} = \pm[\frac{A}{v \cdot (\beta + \gamma)}]^{\frac{1}{n}} \quad (4)$$

In above equations, A is redundant because hysteresis force and stiffness can be adjusted by stiffness ratio α and shape parameters β, γ and n. Hence, in this work the value of A is set to 1 as a matter of convenience.

The stiffness and strength degradation parameters η and v can be expressed as the functions of accumulated hysteresis energy, as shown in Eqs. (5) and (6)

$$\eta(\varepsilon) = 1 + \delta_\eta \cdot \varepsilon \quad (5)$$

$$v(\varepsilon) = 1 + \delta_v \cdot \varepsilon \quad (6)$$

where δ_v and δ_η denote the degradation coefficients for strength and stiffness, respectively; ε denotes the energy obtained by hysteresis component which can be calculated by continuously integrating the hysteresis moment T over the rotation θ

$$\begin{aligned} \varepsilon(t) &= \int_{\theta(0)}^{\theta(t)} T \cdot d\theta \\ &= (1-\alpha) \cdot k_0 \cdot \int_{\theta(0)}^{\theta(t)} y(\theta, t) \cdot dt \cdot \frac{d\theta}{dt} \\ &= (1-\alpha) \cdot k_0 \cdot \int_0^t y(\theta, t) \cdot \dot{\theta}(t) \cdot dt \end{aligned} \quad (7)$$

If the value of δ_η or δ_v is equal to 0, there is no stiffness or strength degradation in the system. With the increase of δ_η, both hysteresis moment and rotational stiffness will be decreased. Different from the effect of δ_η, the increment of δ_v will induce the reducing hysteresis moment, but the rotational stiffness is unchanged.

In Eq. (2), $h(y)$ denotes the pinching function and its mathematical expression is given in Eq. (8).

$$h(y) = 1 - \zeta_1 \cdot \exp\left\{\frac{-[y \cdot \mathrm{sgn}(\dot{\theta}) - q \cdot y_u]^2}{\zeta_2^2}\right\} \quad (8)$$

where ζ_1 affects the pinching severity and its value ranges between 0 and 1; ζ_2 is a parameter to regulate the area where the pinching phenomenon will extend; q is used to adjust the pinching level which is a constant. Both ζ_1 and ζ_2 are the functions of hysteresis energy ε, as shown in Eqs. (9) and (10).

$$\zeta_1(\varepsilon) = \xi_{10} \cdot [1 - \exp(-p \cdot \varepsilon) \quad (9)$$

$$\zeta_2(\varepsilon) = (\psi_0 + \delta_\psi \cdot \varepsilon) \cdot (\lambda + \zeta_1) \quad (10)$$

Table 4 Geometric description of model parameters

No.	Parameter	Geometric description
1	α	Ratio of post-yield to initial rotational stiffness
2	k_0	Initial rotational stiffness
3	c_0	Initial rotational damping
4	β	Hysteresis shape regulation
5	γ	Hysteresis shape regulation
6	n	Hysteresis shape regulation
7	ξ_{10}	Whole slip
8	q	Pinching level
9	p	Pinching slope
10	ψ_0	Pinching amount
11	δ_ψ	Pinching extension rate
12	λ	Pinching severity interaction
13	δ_v	Strength degradation
14	δ_η	Stiffness deterioration
15	T_0	Bending moment offset

where ξ_{10} denotes the whole slip; p controls the rate of the initial drop in the slope; ψ_0 designates the pinching amount; δ_ψ denotes the rate of the pinching extension; λ is a parameter to regulate the variation rate of ζ_2 with the change of ζ_1.

Table 4 gives the geometric description of each parameter of the proposed rotational model that is used to characterize the cyclic behaviour of the composite joint.

3.2 Model parameter identification

In the proposed rotational hysteresis model, there are 15 parameters to be identified, i.e. k_0, c_0, α, β, γ, n, ξ_{10}, q, p, ψ_0, δ_ψ, λ, δ_v, δ_η and T_0. The process of parameter identification can be regarded as solving a global minimization optimization problem, because the parameter values are difficult to be calculated through trials. The key problem for tackling such an optimization problem is to build up a rational fitness function, which is crucial to the accuracy of final identification results. Besides, an obvious feature of the proposed model is that it has the highly nonlinear differential equation (Eq. (2)) in the mathematical expression, which brings about the challenges for parameter calculation. Here, the Runge-Kutta algorithm with four orders is utilized to identify the variable "*y*" via an iterative process. The corresponding process can be expressed by Eqs. (11)-(15).

$$y_{i+1} = y_i + \frac{[z_1 + 2 \cdot (z_2 + z_3) + z_4]}{6} \quad (11)$$

$$z_1 = \Delta t \cdot \begin{bmatrix} \dot{\theta}_i - v \cdot (\beta \cdot |\dot{\theta}_i| \cdot |y_i|^{n-1} \cdot y_i \\ h(y_i) \cdot \dfrac{+\gamma \cdot \dot{\theta}_i \cdot |y_i|^n)}{\eta} \end{bmatrix} \quad (12)$$

$$z_2 = \Delta t \cdot \left[h(y_i + \frac{z_1}{2}) \cdot \frac{\left(\frac{\dot\theta_i + \dot\theta_{i+1}}{2}\right) - v \cdot \begin{pmatrix} \beta \cdot \left|\frac{\dot\theta_i + \dot\theta_{i+1}}{2}\right| \cdot \left|y_i + \frac{z_1}{2}\right|^{n-1} \\ \cdot \left(y_i + \frac{z_1}{2}\right) + \gamma \cdot \left(\frac{\dot\theta_i + \dot\theta_{i+1}}{2}\right) \\ \cdot \left|y_i + \frac{z_1}{2}\right|^{n} \end{pmatrix}}{\eta} \right] \quad (13)$$

$$z_3 = \Delta t \cdot \left[h(y_i + \frac{z_2}{2}) \cdot \frac{\begin{matrix} (\frac{\dot\theta_i + \dot\theta_{i+1}}{2}) - v \cdot (\beta \cdot \left|\frac{\dot\theta_i + \dot\theta_{i+1}}{2}\right| \cdot \left|y_i + \frac{z_2}{2}\right|^{n-1} \\ \cdot (y_i + \frac{z_2}{2}) + \gamma \cdot (\frac{\dot\theta_i + \dot\theta_{i+1}}{2}) \cdot \left|y_i + \frac{z_2}{2}\right|^{n}) \end{matrix}}{\eta} \right] \quad (14)$$

$$\begin{aligned} z_4 = \Delta t \cdot [& h(y_i + z_3) \\ & \dot\theta_{i+1} - v \cdot (\beta \cdot \left|\dot\theta_{i+1}\right| \cdot |y_i + z_3|^{n-1} \\ & \cdot (y_i + z_3) + \gamma \cdot \dot\theta_{i+1} \cdot |y_i + z_3|^{n}) \\ & \cdot \frac{}{\eta}] \end{aligned} \quad (15)$$

where Δt is the sampling rate. Hence, based on calculated time-series y, the fitness function can be defined as the root mean square (RMS) error between experimental results and model outputs, as shown in Eq. (16).

$$\begin{aligned} Obj(x) &= \sqrt{\frac{1}{N_d}\sum_{i=1}^{N_d}[T_{test}(i) - MT(i)]^2} \\ &= \sqrt{\frac{1}{N_d}\sum_{i=1}^{N_d}\begin{Bmatrix} T_{test}(i) - [\alpha \cdot k_0 \cdot \theta_i + c_0 \cdot \dot\theta_i \\ +(1-\alpha) \cdot k_0 \cdot y_i + T_0] \end{Bmatrix}^2} \end{aligned} \quad (16)$$

where *Obj* denotes the fitness function; $X = [k_0, c_0, \alpha, \beta, \gamma, n, \xi_{10}, q, p, \psi_0, \delta_\psi, \lambda, \delta_v, \delta_\eta, T_0]$ denotes the vector of parameters to be identified; T_{test} and MT denote the measured moment in experimental testing and predicted moments from the model, respectively; N_d is the number of data samples used for model identification. Consequently, the model parameter identification is transformed to the minimization of the fitness function, as shown in Eq. (17).

$$\begin{aligned} &\text{Min } Obj(X) \\ &s.t.\ k_0 > 0, \quad c_0 > 0, \quad 0 < \alpha < 1, \\ &\beta > 0, \quad n > 0, \quad \xi_{10} > 0, \\ &q > 0, \quad p > 0, \quad \psi_0 > 0, \quad \delta_\psi > 0, \\ &\lambda > 0, \quad \delta_v > 0, \quad \delta_\eta > 0 \end{aligned} \quad (17)$$

When the fitness value equals to zero, the corresponding X (parameter matrix) will be the optimal parameters of the proposed model. To solve such a problem, the direct and gradient-based search algorithms may not work due to high nonlinearity and indescribable gradient information in the optimization problem. As a result, a modified chicken swarm optimization algorithm is put forward to solve this optimization problem for optimal parameter identification of the proposed rotational hysteresis model.

4. Modified chicken swarm optimization

4.1 CSO description

Chicken swarm optimization (CSO), proposed by Meng *et al*. in 2014 (Meng *et al*. 2014), is a novel heuristic swarm-based optimization algorithm in accordance with food searching of hens, cocks and chicks. Besides the characteristics of traditional swarm intelligence optimization algorithms, the CSO adopts the strategies of population subdivision and collaborative optimization to maximize the global search ability of the algorithm in the solution space. As one of the most common poultry, chicken is a kind of gregarious animal with strong hierarchy. In general, the cock is playing a dominant part in the chicken swarm with stronger food search ability, followed by hens and chicks. Via simulating this social formation, the CSO is employed to resolve the practical optimization problems.

In view of above description, the individuals in the chicken swarm can be simplified as follows.

(1) The whole chicken swarm can be divided into several groups and each group consists of a cock, a few hens and chicks.
(2) The fitness is employed to distinguish the identities of cock, hen and chick in the swarm. The chickens with several optimal fitness values are regarded as the cocks. The chickens with several worst fitness values are considered as the chicks. The rest of the chickens will be the hens in the swarm. The hens are always randomly assigned to each group and the relationships between hens and their chicks are randomly built up as well.
(3) The identities, hierarchical ranking and parent-child relationship of each group in the swarm are kept unchanged and just updated every G times of algorithm iteration.
(4) In each group, the chickens follow the cock (group leader) to search for food, and simultaneously prevent other chickens from eating their own food. Suppose that the chickens are able to randomly steal other chickens' food and the chicks find food around their mothers in the swarm. Hence, the dominant chickens have benefits in the process of food searching.

Suppose there are N chickens in the swarm, in which the numbers of cock, hen and chick are CO_N, H_N and Ch_N, respectively. Let $x_{i,j}^t$ (I = 1, …, N; j = 1, …, D) denote the location of ith chicken at tth iteration in the D-dimensional space. Different types of chicken have different location update strategies, given as follows.

Location update of cock: the cock with better fitness value has wider range to seek for food than other cocks with less fitness. Its location is only affected by other cocks' locations. Hence, the location update formula of the cock is given as follows

$$x_{i,j}^{t+1} = x_{i,j}^t \cdot [Rdn(0, \sigma^2) + 1] \quad (18)$$

where $x_{i,j}$ denotes the location of ith cock at jth dimension; t

denotes the current iteration number; $Rdn(0,\sigma^2)$ denotes a random value with normal distribution of zero mean value and standard deviation of σ^2. The value of σ^2 is determined by the following equation.

$$\sigma^2 = \begin{cases} e^{\frac{f_k - f_i}{\varepsilon + |f_i|}}, & f_i > f_k, \quad k \in [1, N], \quad k \neq i \\ 1, & others \end{cases} \tag{19}$$

where ε is a small constant that is used to avoid aero denominator. f_i denotes the fitness value of ith cock while f_k denotes randomly selected kth cock.

Location update of hen: The hens follow the cocks in their groups to search for food, and in the meantime, they compete with other hens via stealing their food. Therefore, the location of the hen is affected by other cocks and hens. The location update strategy of the hen is formulated as follows.

$$\begin{aligned} x_{i,j}^{t+1} = x_{i,j}^t + c_1 \cdot Rd_1 \cdot \left(x_{r_1,j}^t - x_{i,j}^t\right) \\ + c_2 \cdot Rd_2 \cdot (x_{r_2,j}^t - x_{i,j}^t) \end{aligned} \tag{20}$$

$$c_1 = e^{\frac{f_i - f_{r_1}}{\varepsilon + |f_i|}} \tag{21}$$

$$c_2 = e^{f_{r_2} - f_i} \tag{22}$$

where Rd_1 and Rd_2 denote random numbers between 0 and 1; c_1 represents the influencing factor of r_1th cock in the ith hen's group on ith hen; c_2 denotes the influencing factor of r_2th cock or hen in the swarm on ith hen.

Location update of chick: The chick has the least ability to search for food and can only follow its mother hen in its group for the food. Hence, the location of the chick is just affected by its mother, with the following expression.

$$x_{i,j}^{t+1} = x_{i,j}^t + h_1 \cdot (x_{m,j}^t - x_{i,j}^t) \tag{23}$$

where $x_{m,j}$ denotes the location of mth mother hen at jth dimension; h_1 denotes the influencing factor of mother hen on the chick's location, which is a constant in CSO.

To sum up, the procedure of CSO can be summarized as the following steps.

Step 1. Initialize the chicken population N. Set maximum iteration number N_{ite}, interval generation G, cock number CO_N, hen number H_N and chick number Ch_N.

Step 2. Calculate the fitness value of each chicken in the swarm and set current iteration number $t = 0$.

Step 3. Judge whether current t meets the update condition of chicken identity. If t % G = 0, rearrange the chickens according to their fitness values, re-divide chicken population into different groups and re-establish the hierarchical order and mother-child relationship.

Step 4. Use Eqs. (18)-(23) to update the locations of cocks, hens and chicks in the swarm.

Step 5. Calculate the fitness value of each chicken in the updated swarm. If individual fitness value after updating is better than its previous one, update its location; otherwise, keep previous location unchanged.

Step 6. Update $t = t + 1$. If $t < N_{ite}$, repeat Steps 3-6; otherwise, terminate the algorithm iteration.

4.2 M-CSO algorithm

Despite the fact that CSO has been proved to be effective in the application of engineering optimization, it still has the drawback of the premature convergence when dealing with complex optimization problems. To prevent the algorithm from early trapping into the local optimum, a modified CSO (M-CSO) is developed in this study to improve the identification accuracy. In the CSO, the chicks are as important as cocks and hens in food searching. Accordingly, the main idea of M-CSO is to improve location update mechanism of chicks in the swarm. In the original CSO, the location of the chick is only affected by its mother hen. When the mother is located near local optimal location, the child is more prone to be trapped in local optimal location. However, in practice, the chick not only follows its mother to find food, but also refers to the location of the cock, which is the most dominant in the group. Hence, in the location update formula of the chick, a self-learning factor w and an influencing factor c_3 are added to Eq. (23), shown as follows.

$$\begin{aligned} x_{i,j}^{t+1} = w \cdot x_{i,j}^t + h_1 \cdot \left(x_{m,j}^t - x_{i,j}^t\right) \\ + c_3 \cdot (x_{r,j}^t - x_{i,j}^t) \end{aligned} \tag{24}$$

$$w + c_3 = 1 \tag{25}$$

where c_3 represents the location influence from rth cock in the swarm. Moreover, the influencing factor h_1 is always defined as a constant. If h_1 is assigned with a big value, the algorithm will have better global search ability but worse local search ability. Conversely, if h_1 is assigned with a small value, the algorithm will have better local search ability but worse global search ability. It is challenging to balance both global and local search abilities in the algorithm iteration procedure to speed up the convergence and improve identification accuracy in the meantime. In this study, a self-adaptive h_1 will be introduced in location update of the chick, which starts with a high value to make the algorithm rapidly converge to approximate location of global optimum and gradually decreases to a small value to improve the result accuracy in the later stage of iteration via enhancing local search ability. There are a large number of choices for mathematical expression of self-adaptive decreasing h_1, including both linear and nonlinear expressions. Here, a nonlinear expression is employed to automatically adjust the value of h_1 during the evolutionary procedure, shown in Eq. (26).

$$h_1 = h_1^{\min} + (h_1^{\max} - h_1^{\min}) \cdot e^{\alpha \cdot (\frac{t}{N_{ite}})^{\beta}} \tag{26}$$

where $[h_1^{\min}, h_1^{\max}]$ denotes the range of h_1; α and β are two parameters to regulate the curve. In this study, α = -20 and β = 5 due to the perfect feature of symmetry. Fig. 10 gives an example of decreasing h_1 comparison between linear and nonlinear cases. It is clearly seen that nonlinear decreasing h_1 is better than linear one, as it can keep maximum value of h_1 for a long time in the initial period of optimization and quickly decline to its minimum value at the later stage. Accordingly, both exploration and exploitation abilities of

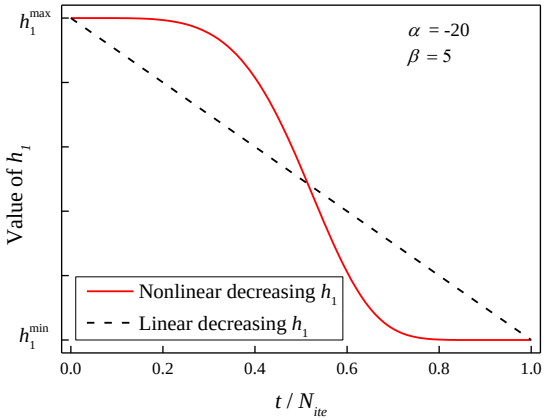

Fig. 10 Comparison between linear and nonlinear decreasing h_1

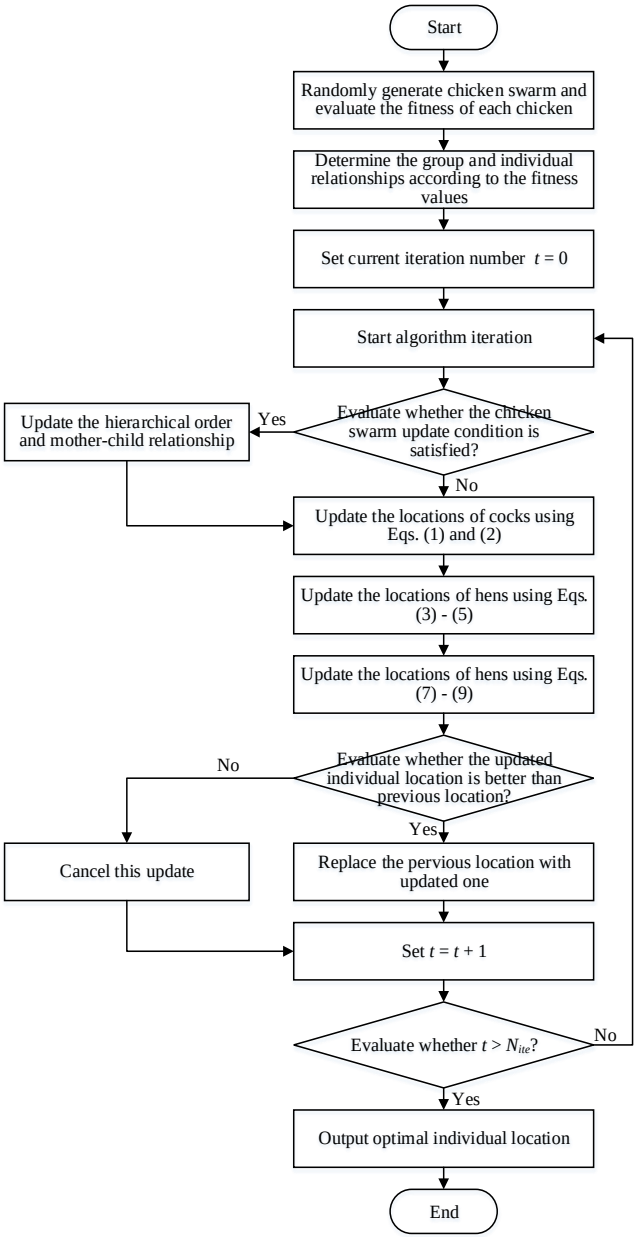

Fig. 11 Flowchart of M-CSO

the CSO algorithm are enhanced. Based on these modifications, the procedure of M-CSO can be illustrated by the flowchart in Fig. 11.

4.3 Algorithm performance evaluation

In this section, four benchmark functions are employed to test the performance of the proposed M-CSO via a comparison with other commonly used swarm-based optimization algorithms. Here, both identification accuracy and convergence rate are considered as algorithm evaluation indices. Table 5 gives the details of four benchmark test functions, including Griewangk function (F1), Rastrigrin function (F2), Rosenbrock function (F3) and Schewefel function (F4), which are able to comprehensively evaluate the algorithm performance. Fig. 12 shows corresponding two-dimensional (x) graphs of four functions. It is clearly seen that all the functions are nonlinear multi-modal functions with a large number of local optimal solutions, and they have global optimal solution with value of 0. In this study, the optimization dimension is set as 20. Besides the proposed M-CSO, particle swarm optimization (PSO), fruit fly algorithm (FFA) and standard CSO are adopted to solve the optimization problems of the test functions. To make a fair comparison, the swarm size and maximum iteration number are set as 40 and 500 for all the optimization algorithms. Other parameter settings of algorithms are provided as follows: in the PSO, the inertia weight is set as 0.85 and two learning factors are set as 1.5 (Das *et al*. 2018, Ho-Huu *et al*. 2018); in the FFA, the searching step is in the range of [-1, 1]; in the CSO and M-CSO, the number of cocks is 6, the number of hens is 28, the number of chicks is 6, w = 0.6, and c_3 = 0.4.

Then, the PSO, FFA, CSO and M-CSO are adopted to optimize four test functions. All algorithms are programmed using Matlab v.2016a. For each algorithm and each function, 50 independent tests were conducted, and used to record and calculate the minimum fitness, maximum fitness, mean fitness, standard deviation of fitness and mean running time. Table 6 shows the test results of different optimization algorithms. From the optimization results of F1, the optimal fitness values of CSO and M-CSO are 0, which is the target of the optimization problem. The optimal fitness values of PSO and FFA are 0.0059 and 0.0014, respectively. Hence, the optimization capacities of CSO and M-CSO are obviously better than that of PSO and FFA. Compared with CSO, the M-CSO has optimal mean fitness and standard deviation, which proves outstanding stability and robustness. Similar to results of F1, the results of F2, F3 and F4 also validate that the M-CSO outperforms PSO, FFA and CSO in terms of minimum fitness, maximum fitness and solution stability, even though it requires more time for solving the optimization problem than PSO and FFA. The mean running time of both CSO and M-CSO is in the range of [1.3, 1.5] s, which demonstrates that the modified version of CSO is capable of effectively improving the algorithm accuracy without adding any calculation cost.

Table 5 Details of benchmark test functions

Function	Expression	Dimension	Range	Target
Griewangk (F1)	$\sum_{i=1}^{N}\frac{x_i^2}{4000}-\prod_{i=1}^{N}\cos(\frac{x_i}{\sqrt{i}})+1$	20	[-10,10]	0
Rastrigrin (F2)	$10\cdot N+\sum_{i=1}^{N}[x_i^2-10\cdot\cos(2\cdot\pi\cdot x_i)]$	20	[-10,10]	0
Rosenbrock (F3)	$\sum_{i=1}^{N-1}[100\cdot(x_i^2-x_{i+1})^2+(1-x_i)^2]$	20	[-10,10]	0
Schewefel (F4)	$\sum_{i=1}^{N}\lvert x_i\rvert+\prod_{i=1}^{N}\lvert x_i\rvert$	20	[-10,10]	0

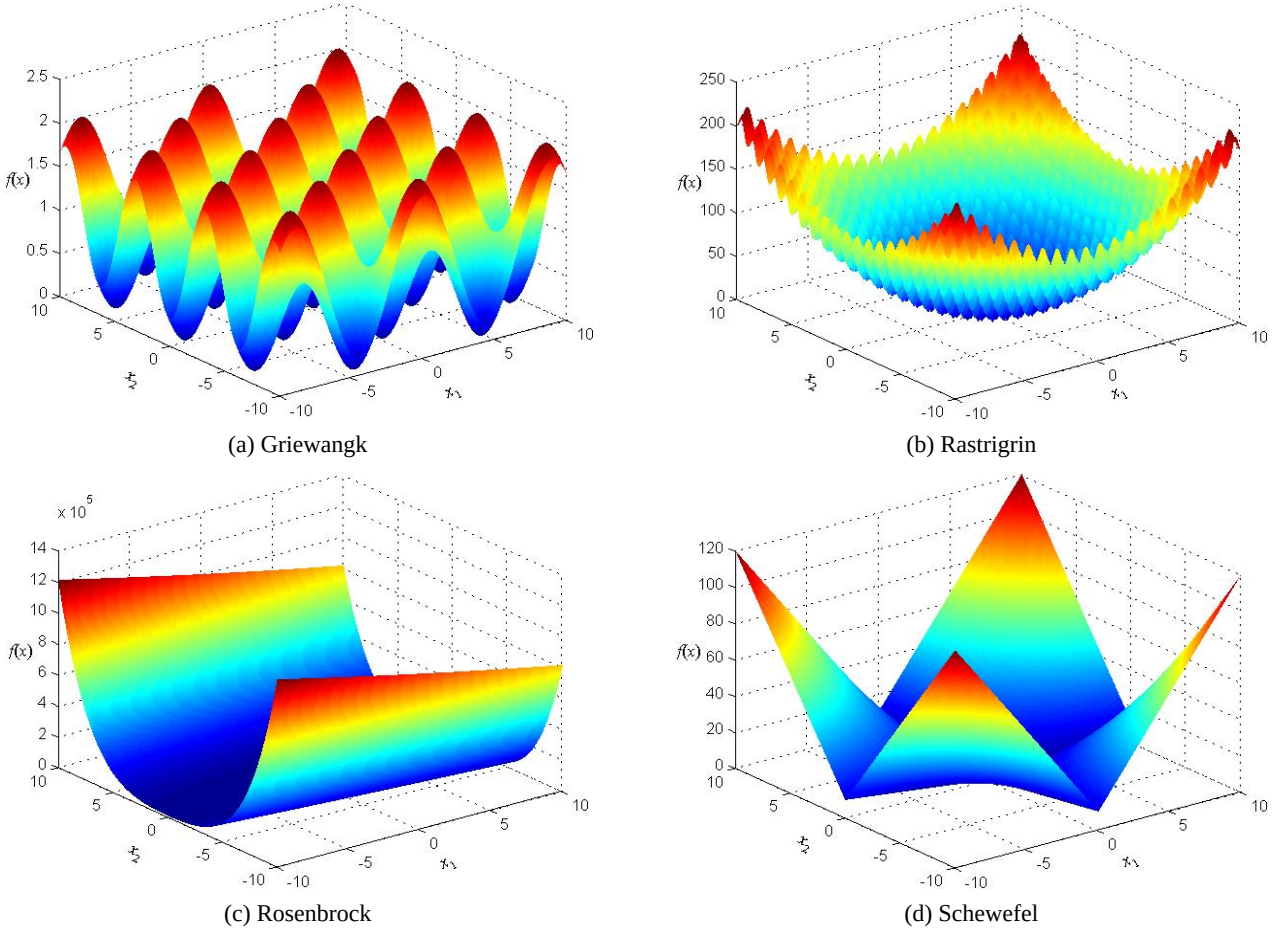

(a) Griewangk (b) Rastrigrin

(c) Rosenbrock (d) Schewefel

Fig. 12 Plots of 2-D benchmark test functions

To better evaluate the convergence rate and accuracy of each algorithm, the fitness variations of four algorithms during the evolutionary process are also compared, as shown in Fig. 13. It is clearly noted that the proposed M-CSO algorithm has the fastest convergence and best accuracy compared with other three algorithms, which fall into the local optimums for a period to different degrees. The M-CSO, however, has the ability of avoiding trapping into the local optimum and can accurately find the optimization target in a short time.

5. Identification results and analysis

5.1 Modeling results

To appraise the capacity of the proposed rotational hysteresis model to predict the cyclic behavior of the composite joints, the measured data from five specimens are employed to identify the best model parameter values. The parameter values of M-CSO are the same as that of M-CSO in Section 4.3. The optimal parameter values of the

Table 6 Test results of different algorithms

Index	Algorithm	Minimum fitness	Maximum fitness	Mean fitness	Standard deviation	Mean time (s)
F1	PSO	0.0059	0.1758	0.0599	0.0024	0.1692
	FFA	0.0014	0.3516	0.0217	0.0031	0.0735
	CSO	0	0.1246	0.0261	0.0009	1.4398
	M-CSO	0	8.41E-06	7.04E-11	2.41E-24	1.4524
F2	PSO	7.1903	75.2250	25.2108	512.8166	0.1962
	FFA	5.8382	8.2734	7.1649	0.2816	0.1103
	CSO	1.6148	12.7440	5.5184	47.3729	1.3974
	M-CSO	0	2.3876	1.3734	3.4481	1.3911
F3	PSO	7.7626	12.7392	9.4148	0.9249	0.2192
	FFA	3.2369	9.0972	5.4321	2.2351	0.1024
	CSO	2.8291	6.2484	4.1492	0.6314	1.4038
	M-CSO	9.91E-05	1.9867	0.9778	0.3076	1.4005
F4	PSO	0.1853	1.1231	0.5735	0.0401	0.1973
	FFA	0.0430	0.04147	0.0422	1.16E-07	0.0974
	CSO	1.22E-23	3.17E-27	1.32E-24	7.77E-48	1.3732
	M-CSO	2.21E-31	8.61E-50	5.61E-33	1.22E-63	1.3729

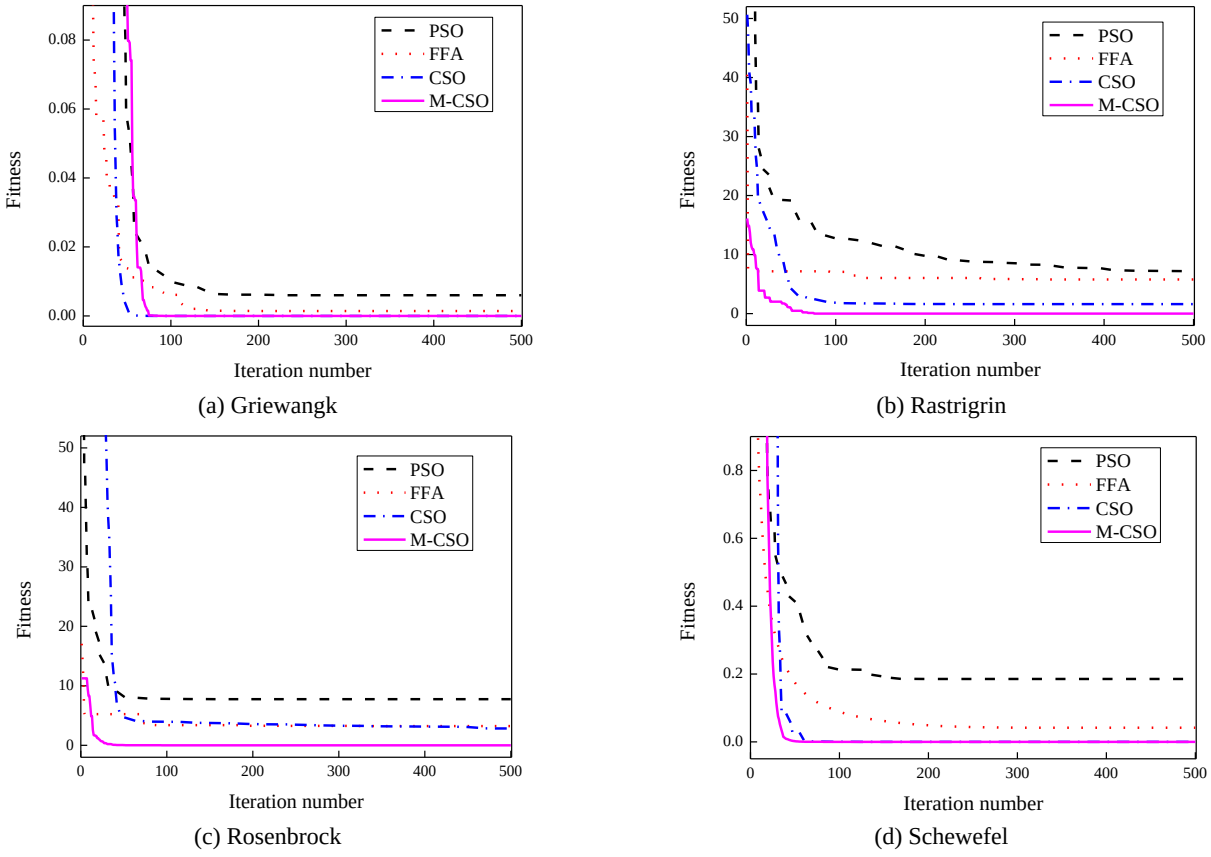

(a) Griewangk (b) Rastrigrin

(c) Rosenbrock (d) Schewefel

Fig. 13 Algorithm iteration process

proposed model for the composite joints are summarized in Table 7. Figs. 14(a)-18(a) show the hysteretic loop comparisons between experimental results and model predictions for five composite joints, respectively, in which the solid blue lines represent measured moments by the testing and the red dotted lines denote the predicted moments from the proposed model. It is noticeable from the figures that with the increase of loading amplitude, the

Table 7 Parameter identification results of the five specimens

Parameter		k_0	c_0	α	β	γ	n	ξ_{10}
ID	S-1	5.9130	2.6758	0.0018	0.0116	0.0141	1.0395	0.3527
	S-2	4.9564	1.8798	0.0663	0.0249	0.0013	1.0000	0.8452
	S-3	5.0485	1.2356	0.0442	0.0205	0.0131	1.0001	0.3266
	S-4	5.9389	2.7568	0.0712	0.0192	0.0076	1.0005	0.0269
	S-5	5.8977	3.3775	0.0659	0.0193	0.0058	1.0001	3.8×10^{-6}
Parameter		q	p	ψ_0	δ_ψ	λ	δ_ν	δ_η
ID	S-1	0.0010	0.0422	0.0355	0.0009	0.3283	8.2×10^{-5}	1.6×10^{-5}
	S-2	0.0003	1.4×10^{-10}	0.0266	0.0003	0.1145	0.0001	4.9×10^{-5}
	S-3	0.0040	0.2688	0.0593	0.0008	0.4999	4.5×10^{-5}	8.9×10^{-10}
	S-4	0.0009	0.3563	0.0279	0.0001	0.0299	0.0001	2.1×10^{-5}
	S-5	0.4259	0.2993	0.0295	0.0010	0.0583	0.0002	4.2×10^{-5}

phenomenon of stiffness and strength degradations become more obvious. And the good agreements between two types of hysteresis loops effectively prove the outstanding ability of the proposed model to capture the nonlinear behaviour of the composite joints under cyclic loading. To further quantify the model prediction accuracy, the Pearon's correlation coefficient (R) between measured and predicted moments is also employed for model assessment, the formula of which is given in Eq. (27).

$$R = \frac{N_d \cdot \left[\sum_{i=1}^{N_d} MT(i) \cdot T_{test}(i)\right] - \left[\sum_{i=1}^{N_d} MT(i)\right] \cdot \left[\sum_{i=1}^{N_d} T_{test}(i)\right]}{\sqrt{\left\{N_d \cdot \sum_{i=1}^{N_d} MT(i)^2 - \left[\sum_{i=1}^{N_d} MT(i)\right]^2\right\} \cdot \left\{N_d \cdot \sum_{i=1}^{N_d} T_{test}(i)^2 - \left[\sum_{i=1}^{N_d} T_{test}(i)\right]^2\right\}}} \quad (27)$$

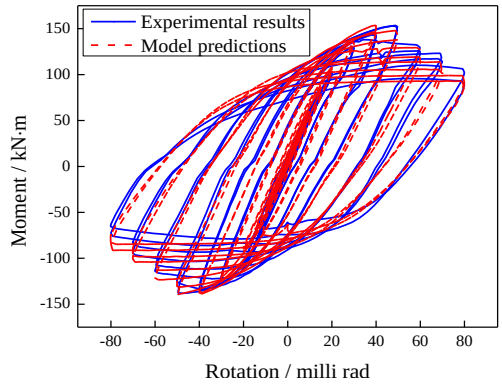

(a) Hysteresis loop

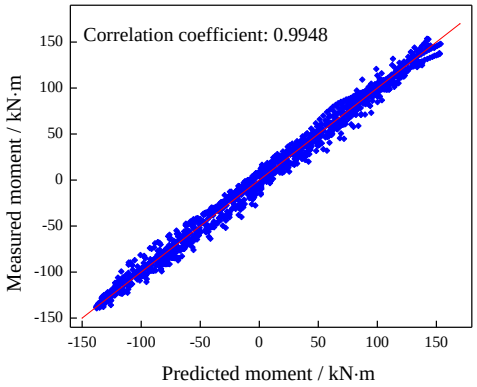

(b) Correlation analysis

Fig. 14 Response comparison of S-1 between experimental results and model predictions

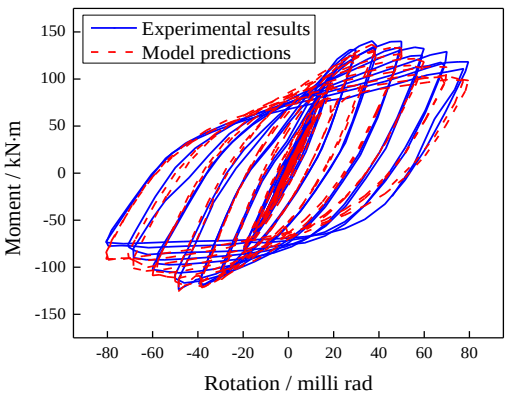

(a) Hysteresis loop

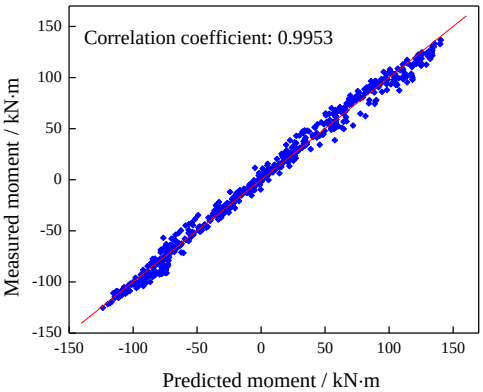

(b) Correlation analysis

Fig. 15 Response comparison of S-2 between experimental results and model predictions

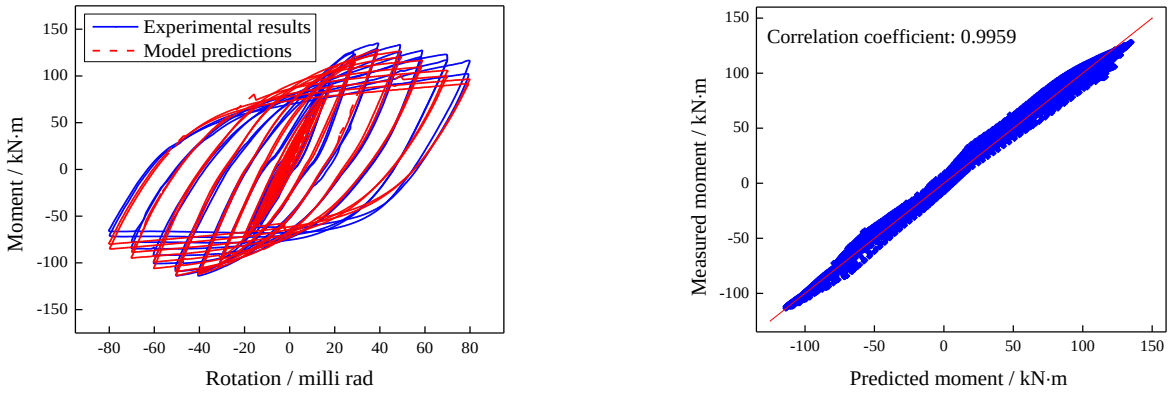

(a) Hysteresis loop (b) Correlation analysis

Fig. 16 Response comparison of S-3 between experimental results and model predictions

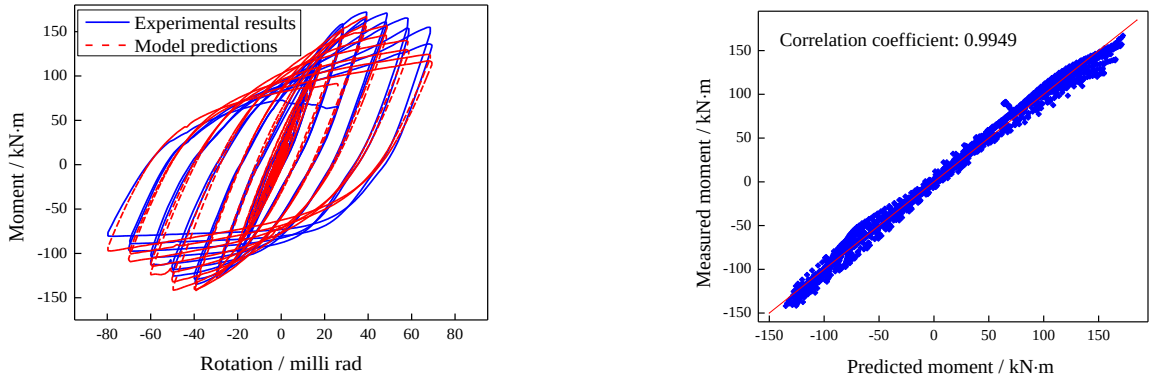

(a) Hysteresis loop (b) Correlation analysis

Fig. 17 Response comparison of S-4 between experimental results and model predictions

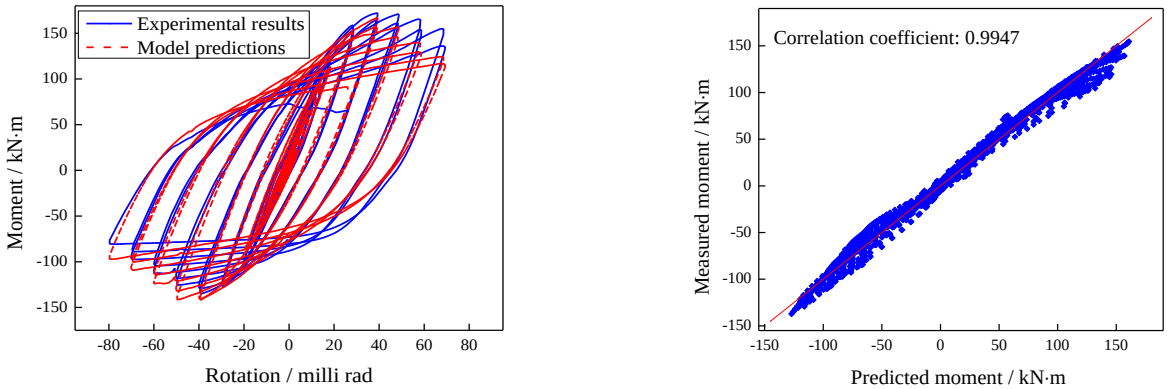

(a) Hysteresis loop (b) Correlation analysis

Fig. 18 Response comparison of S-5 between experimental results and model predictions

where T_{test} and MT denote the experimentally measured moment and predicted moments from the model, respectively, and N_d is the number of data samples. In general, the correlation coefficient higher than 0.95 indicates a satisfactory level of accuracy for the modeling task. Figs. 14(b)-18(b) indicate the correlation analysis results of the proposed rotational hysteresis model for characterizing different joint specimens. It is clearly seen that all the points are uniformly scattered around the line $y = x$ and the values of the correlation coefficient are above 0.99 for all five cases, which indicates the high prediction accuracy of the model to forecast the cyclic behavior of different composite joints.

5.2 Performance analysis

5.2.1 Skeleton curve

Skeleton curve is a good indicator to represent the strength degradation, stiffness deterioration and ductility performance (flexural capacity) of the structure, which can

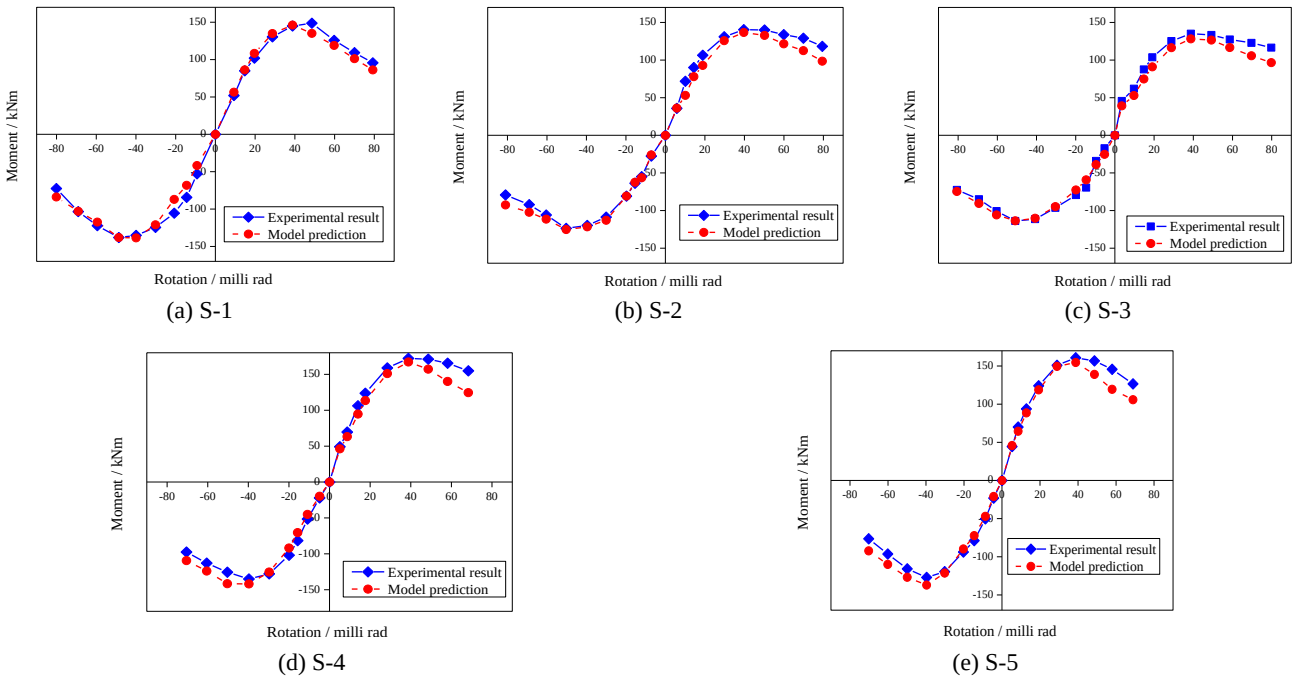

(a) S-1 (b) S-2 (c) S-3

(d) S-4 (e) S-5

Fig. 19 Skeleton curve comparison between experimental results and model predictions

be obtained via extracting the points with maximal values of the loading at each cycle of moment-rotation hysteretic loop and then connecting them together in turn. Fig. 19 displays the comparisons of skeleton curves between experimental results and model predictions for all five joint specimens. It is clearly observed that all the skeleton curves grow in an almost linear manner until they arrive at the yielding points, which indicates that the skeletons will change from the elastic state to the plastic state. After that, structural lateral stiffness, represented by the slope of the curve, starts to reduce, and at the same time, the strength of the specimen begins to decrease after reaching its maximum loading point, and the strength degradation continues until the failure of the structure. By and large, except for some increasing errors in the latter loading stage, the skeleton curves predicted from the proposed model are in good agreement with the experimental results, which represents the model capacity to capture this important indicator.

5.2.2 Strength degradation

The maximum moment of the joint specimen, at the same rotation level during the cyclic loading, will be gradually reduced due to accumulated damage, the phenomenon of which is regarded as the strength degradation. Generally, the strength degradation is characterized using a strength degradation factor, which is defined as follows

$$Stren_j = \frac{T_j^i}{T_j^1} \tag{28}$$

where T_j^i and T_j^1 denote the maximal moments at 1st and ith loading cycles, when the loading rotation is j. Here, the capacity of the proposed model to demonstrate the strength degradation phenomenon is investigated through a comparison between model predictions and experimental results. The corresponding results are shown in Fig. 18. It is noted that the strength degradation factors of all five specimens reduced rapidly and dramatically with the addition of the drift ratio because of the accumulated damage. Before the peak strengths are reached, the values of strength degradation factor are higher than 0.95 and 0.98 for hogging and sagging conditions, respectively, which indicates weak and minor strength deterioration. Then, the values of strength degradation factors will continuously drop off after the maximal strengths are achieved. When the beam flanges are at failure, the strength degradation factor will sharply decrease, as shown in Fig. 20. The comparison results sufficiently demonstrate that the proposed model can depict these features of strength degradation, even if several obvious deviations exist in the early stages of the loading.

5.2.3 Stiffness deterioration

Similar to the strength degradation, stiffness deterioration is another major phenomenon of the composite joints under cyclic loading. Hence, it is of great importance to evaluate the performance of the model to illustrate this characteristic. In tis study, the degree of the stiffness deterioration can be evaluated using the stiffness deterioration factor, which is defined in the following equation (Wang *et al*. 2009)

$$Stif_j = \frac{\sum_{i=1}^{n} PL_j^i}{\sum_{i=1}^{n} Pd_j^i} \tag{29}$$

where PL_j^i denotes the maximum value of applied loading at ith cycle, Pd_j^i denotes the maximum value of the drift at ith cycle, and n represents the number of loading cycles.

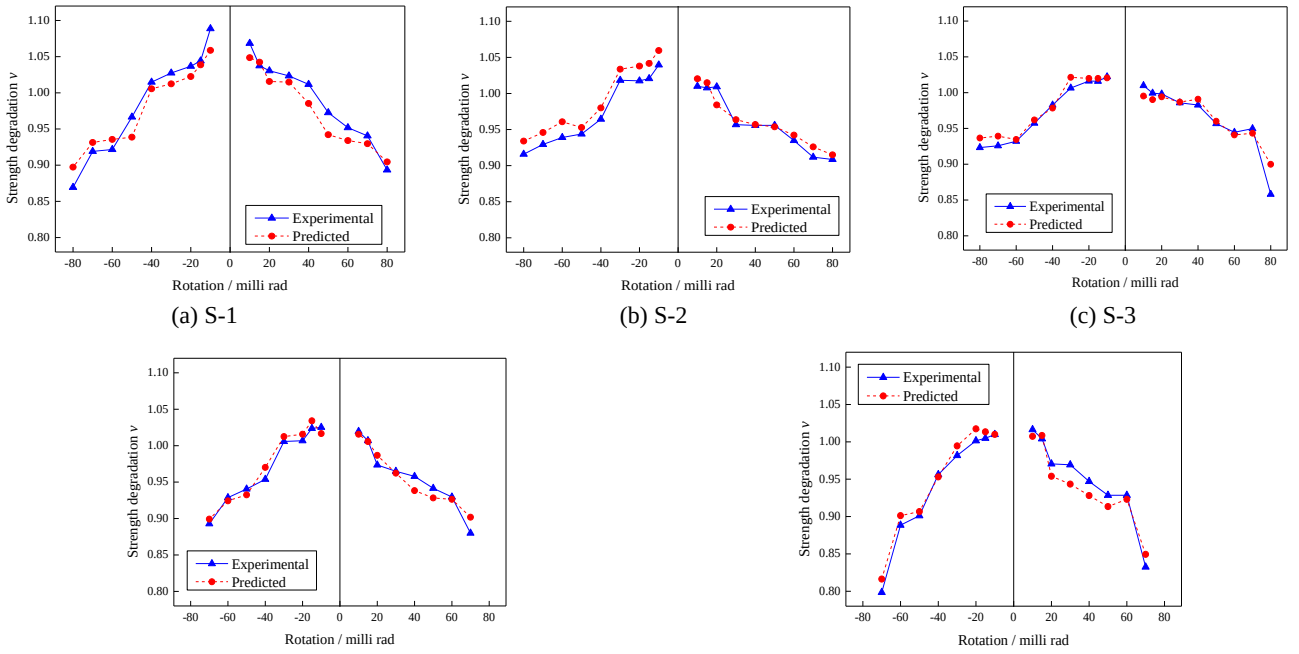

(a) S-1 (b) S-2 (c) S-3

(d) S-4 (e) S-5

Fig. 20 Strength degradation comparison between experimental results and model predictions

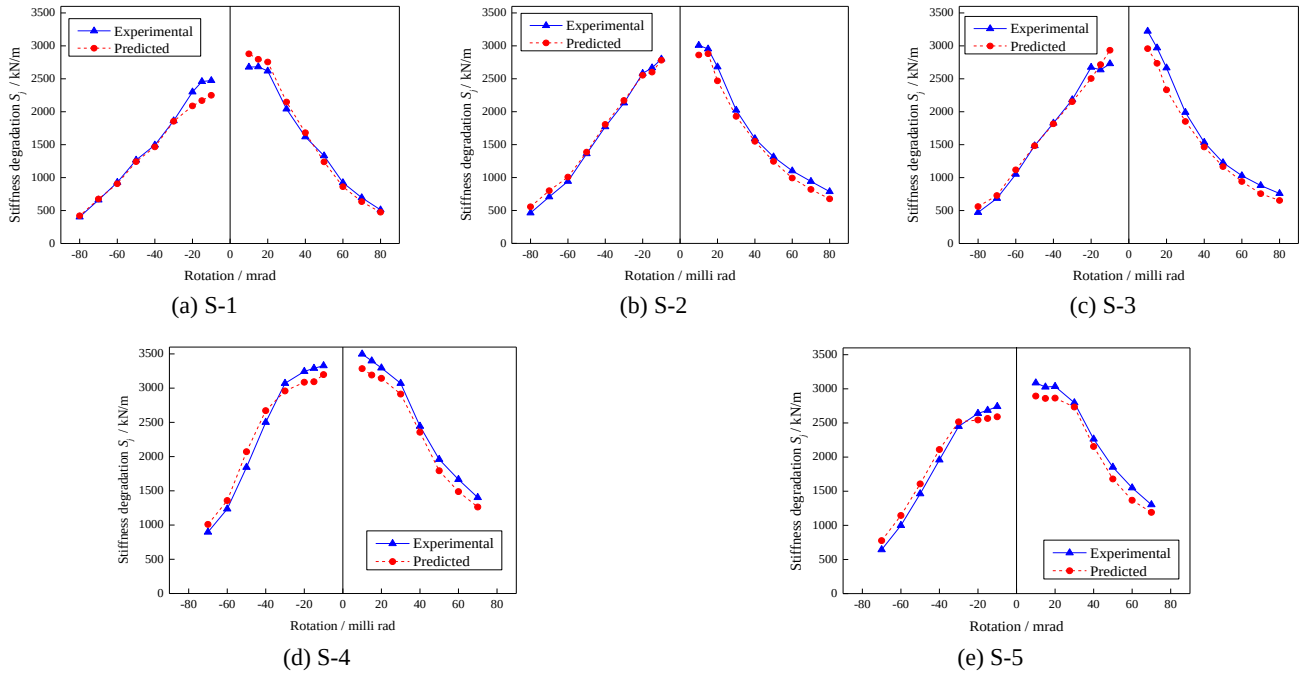

(a) S-1 (b) S-2 (c) S-3

(d) S-4 (e) S-5

Fig. 21 Stiffness deterioration comparison between experimental results and model predictions

The comparisons of stiffness deterioration factors/ rotations relationships between the experimental results and the predictions from the proposed model for all five joint specimens are shown in Fig. 21. It is noticeable that the effect of the slab on the stiffness deterioration of the specimen is similar to that on the reduction of the strength. Because of the RBS contribution, the S-5 under hogging condition has similar variation tendency as the S-1 in developing the stiffness deterioration. However, the flexural stiffness of the S-1 is smaller than that of the S-5 under sagging moment due to the presence of the slab. On the other hand, the height of the steel and the depth of the RBS cut have certain impact on the joint stiffness deterioration. The stiffness deteriorations of the S-2 and S-3 are slightly slower than that of the S-4 and S-5. The main reason for this phenomenon is that the higher the beam is, the more effective plasticity will be generated at the same rotation level. Overall, on account of comparisons between experiential and predicted results, the proposed rotational hysteresis model is capable of effectively capturing these

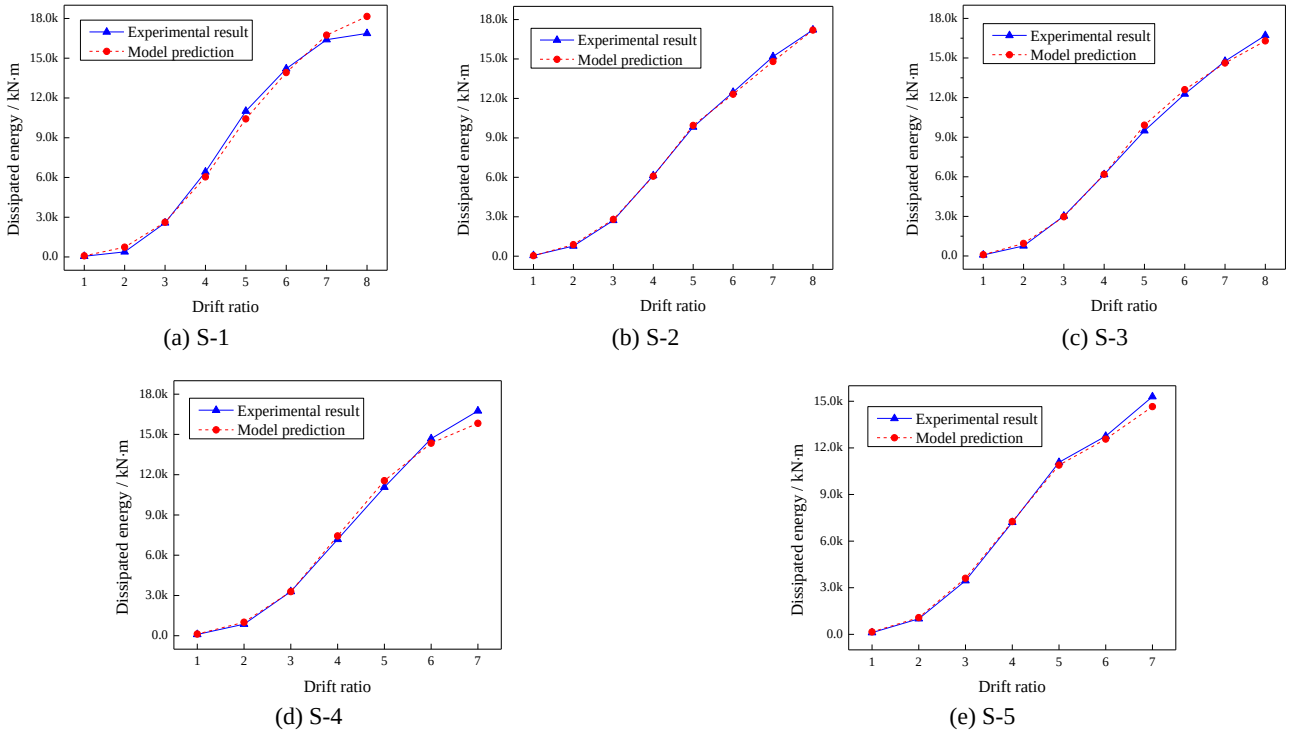

(a) S-1 (b) S-2 (c) S-3

(d) S-4 (e) S-5

Fig. 22 Comparison of energy dissipation between experimental results and model predictions

characteristics of the five joint specimens in terms of stiffness deterioration.

5.2.4 Energy dissipation

The ability for energy dissipation is also important to the performance evaluation of the composite joints, which can be evaluated by the enclosed area under the hysteresis loop. Generally, the larger the enclosed area of the hysteresis loop, the better the seismic performance of the composite joint. Fig. 22 shows the comparisons of energy dissipations calculated from experimental data and model predictions for all five joint specimens, respectively. It is noticeable that with the adding of storey shift ratio, the energy absorbed at each loading cycle is increased accordingly. The main factor contributing to this phenomenon is that after steel yielding, the flexural deformations of the joints will be increased moderately, leading to more absorbed energy. It can be observed from the figures that all the specimens start with absorbed energy of around 100 N·m at the drift ratio of 1, and finally arrive at the maximum energy of around 16,000 N·m before the failure of the joints. This finding demonstrates that the presence of the RBS and slab has limited influence on the change of dissipated energy. Five groups of comparisons validate the performance of the proposed model to predict the energy dissipation of the composite joints under cyclic loading. Especially, in the initial stage of the loading, the predicted absorbed energies resemble the experimental results very well.

5.3 Model parameter analysis

To better utilize the proposed rotational hysteresis model to characterize cyclic behavior of the composite joints, a numerical investigation is carried out to evaluate the effects

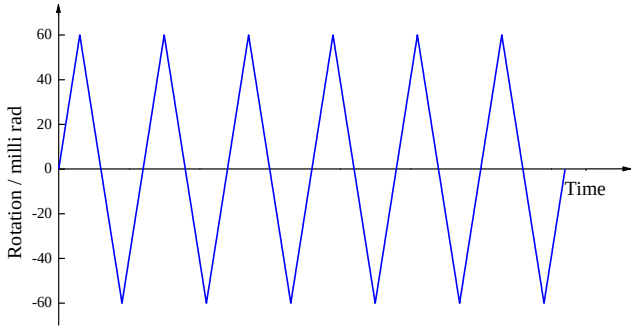

Fig. 23 Cyclic loading simulated for parametric study

of the parameters of the model on the moment outputs. In this study, the reference parameters are set as: $k_0 = 5$, $c_0 = 1$, $\alpha = 0.05$, $\beta = 0.02$, $\gamma = 0.01$, $n = 1$, $\xi_{10} = 0$, $q = 0.1$, $p = 0.2$, $\psi_0 = 0.1$, $\delta_\psi = 0.001$, $\lambda = 0.5$, $\delta_\nu = 0.0005$ and $\delta_\eta = 0.00005$. The cyclic loading is simulated and shown in Fig. 23. Fig. 24 gives the comparison results of moment-rotation hysteretic loops with regard to different values of model parameters k_0, c_0, α, β, γ, n, ξ_{10}, q, p, ψ_0, δ_ψ, λ, δ_ν and δ_η, respectively. It can be observed from Figs. 24(a) and (c) that with the addition of the parameter value, the slopes of the hysteresis loops will be increased accordingly, which indicates that k_0 and α are parameters directly affecting the stiffness of the structure. The influence of c_0 on the output hysteretic loops is illustrated in Fig. 24(b). Unlike k_0 and α that have a certain impact on the slope of the loops, c_0 will contribute to the enlarged enclosed area with the increase of its value, which improves energy dissipation ability. As mentioned in Section 3, the parameters γ, β and n are related to the hysteresis curve, in which n controls the loop smoothness and the combination of β and γ is responsible

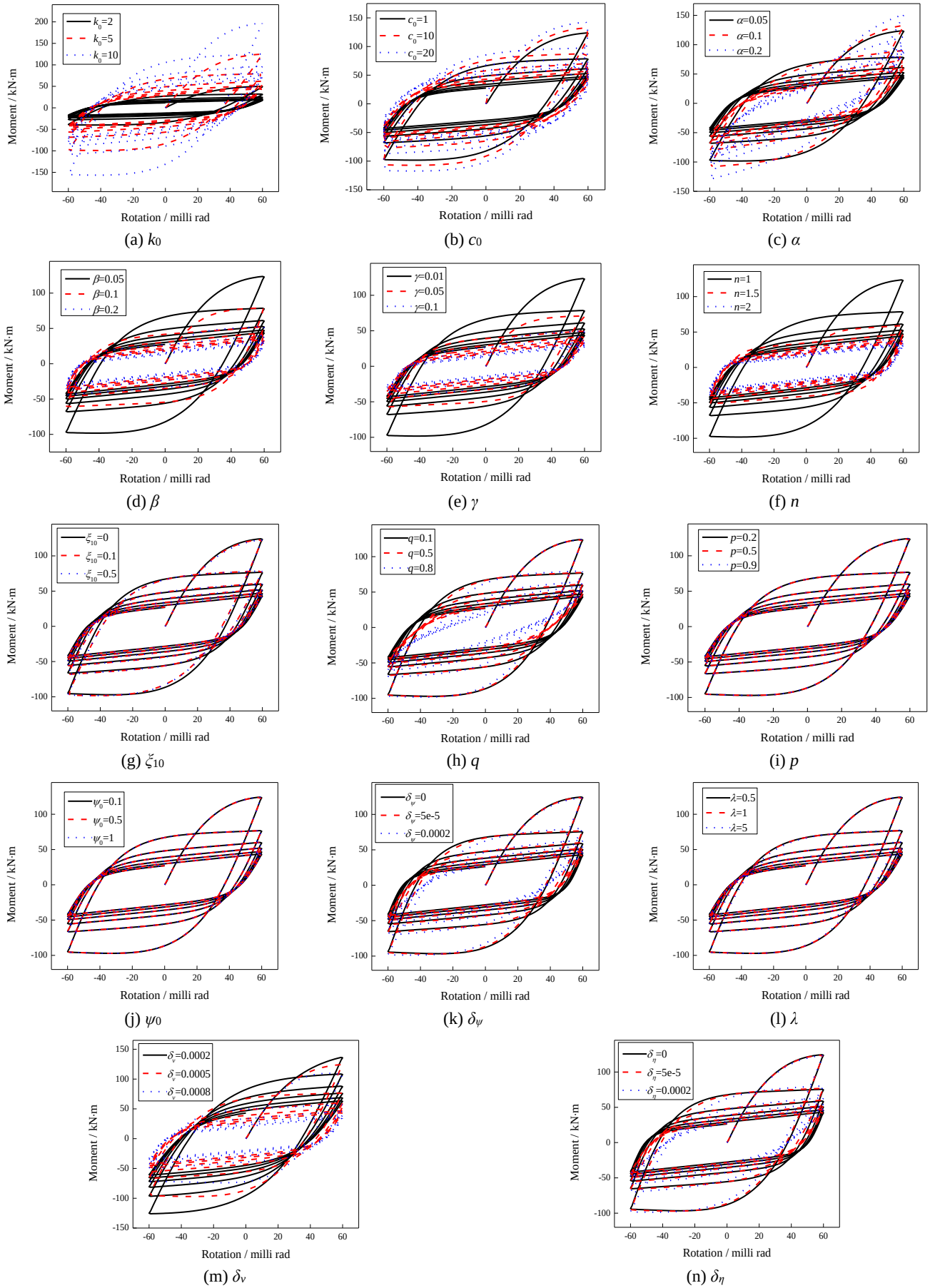

(a) k_0 (b) c_0 (c) α

(d) β (e) γ (f) n

(g) ξ_{10} (h) q (i) p

(j) ψ_0 (k) δ_ψ (l) λ

(m) δ_ν (n) δ_η

Fig. 24 Effect of model parameter on moment output

for the shape of the loop. And Figs. 24(d)-(f) well demonstrate how the values of γ, β and n could affect the shape of the hysteretic loop, respectively. As can be found in Fig. 24(g), the parameter ξ_{10} is used to regulate the slip scale of the hysteretic loop. When the value of ξ_{10} is zero, there is no slip in the hysteretic loop. However, with the ascending value of ξ_{10}, the slip phenomenon can be gradually observed in the loop. q is a constant coefficient to govern the pinching level of the hysteretic loop and Fig. 24(h) portrays how the variation of q affects the hysteretic loops. When q is set as 0.1, no pinching can be found in the loops whilst with the increment of q, more and more obvious pinching is observed in the loops. For parameters p, ψ_0 and λ, changing their values while keeping other parameters unchanged will not generate obvious changes in the hysteretic loops, which is noticeable in Figs. 24(i), (j) and (l). Besides, with the increasing value of parameter δ_ψ, the pinching area extends accordingly, as depicted in Fig. 24(k). Parameters δ_ν and δ_η are responsible for the stiffness and strength deteriorations, and the system will undergo more degradation with the increase of their values, as shown in Figs. 24(m) and (n). In short, the skeleton curve of response loops is determined by the structural property parameters k_0, c_0 and α as well as hysteretic loop parameters γ, β and n. The pinching phenomenon including pinching spread as well as pinching and slope magnitude is regulated by parameters ξ_{10}, q and δ_ψ. The stiffness and strength degradations are governed by parameters δ_ν and δ_η. Consequently, by reasonably adjusting different model parameters, one is capable of satisfying various requirements for characterization of the composite joints.

To effectively assess the effect of the model parameter variation on the output and simplify the expression of the proposed rotational hysteresis model, a sensitivity analysis is conducted in this section. The reference values of model parameters in this case are selected from the specimen S-3, that is k_0 = 5.0485, c_0 = 1.2356, α = 4.5×10^{-5}, β = 0.0205, γ = 0.0131, n = 1.0001, ξ_{10} = 0.3266, q = 0.0040, p = 0.2688, ψ_0 = 0.0593, δ_ψ = 0.0008, λ = 0.4999, δ_ν = 0.0005 and δ_η = 8.9×10^{-10}. During the analysis, each parameter is changed from -50% to 50% of its reference value with an increment of 10% and at the same time other parameter values remained unchanged. Then, the mean RMS errors between the responses with varied parameters and with reference parameters are evaluated and the corresponding RMS error percentage of each parameter is calculated as well. Finally, the sensitivities of model parameters are ranked in the sequence of decreasing percentages. Fig. 25 shows the parameter sensitivity analysis results of the proposed rotational hysteretic model, where a spider chart is used to indicate the RMS error variation of each parameter. Table 8 shows the parameter sensitivity ranking of the proposed model for composite joints in accordance with descending averaged RMS percentages. It is clearly seen that parameters k_0, with the percentage of 32.89%, is the most sensitive parameter in the proposed model followed by n and β with RMS percentages of 21.68% and 18.08%, respectively. In the sensitivity analysis, the model parameters with percentages higher than 3% are generally

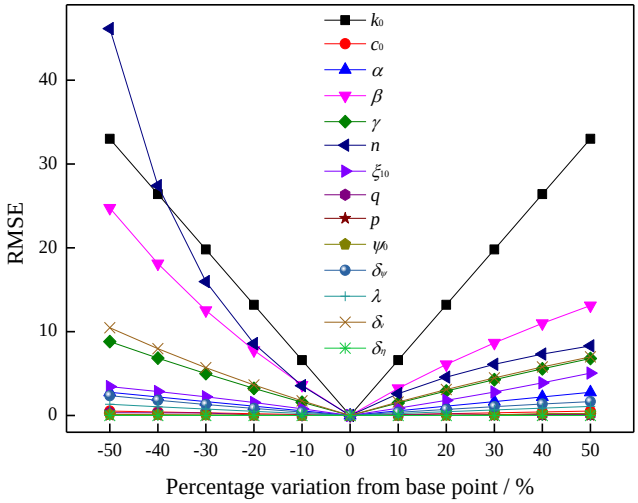

Fig. 25 Sensitivity analysis results of parameters in the proposed model

Table 8 Sensitivity rank of model parameters

Parameter	Mean RMSE	Proportion	Rank
k_0	18.0087	32.89%	1
c_0	0.2851	0.52%	10
α	1.5101	2.76%	7
β	9.9003	18.08%	3
γ	4.2274	7.72%	5
n	11.8773	21.68%	2
ξ_{10}	2.2989	4.20%	6
q	0.1440	0.26%	11
p	0.0091	0.02%	13
ψ_0	0.0871	0.16%	12
δ_ψ	1.0816	1.98%	8
λ	0.6549	1.20%	9
δ_ν	4.6801	8.55%	4
δ_η	0.0001	0.0002%	14

regarded as sensitive parameters. Consequently, k_0, β, γ, n, ξ_{10} and δ_ν are sensitive parameters in the proposed model, because they will result in rational RMS errors when their values diverge from the reference values. Conversely, for c_0, α, q, p, ψ_0, δ_ψ, λ and δ_η, the mean RMS error percentages of which are below 3%, belong to insensitive parameters in the proposed model. These parameters will have less contribution to the model output, even if their values are proportionally varied from the baseline. As a result, the values of insensitive parameters can be set as constants in any numerical study to decrease the number of the model parameters to be identified and then the developed rotational hysteresis model of composite joints will possess the characteristics of feasibility and practicality in engineering applications.

6. Conclusions

This paper presented a numerical method to predict cyclic behavior of the composite joints based on a novel rotational hysteresis model. The proposed predictive model, consisting of a rotational stiffness element, a rotational damping element and a modified Bouc-Wen element, is capable of capturing the unique features of the composite joints such as strength and stiffness deteriorations as well as pinching. Then, the model parameters were identified using chicken swarm optimization algorithm based on experimental results. To improve the modeling accuracy, the chicks' locations in the swarm were updated using both cocks and hens' information, avoiding the algorithm trapping into local optimum. Four benchmark functions have been employed to validate the superiority of the M-CSO in terms of algorithm convergence and accuracy. Finally, five joint specimens with different designs were tested in the laboratory and the experimental results were used in the proposed hysteresis model for parameter identification. The identification results have indicated that the model can not only provide the moment response prediction of the specimens with high accuracy, but also perfectly capture the unique characteristics of the composite joints under cyclic loading such as stiffness and strength degradations as well as energy dissipation. Finally, a parametric study was carried out to investigate the influence of each parameter on the output of the proposed model and identify insensitive parameters that can be eliminated to simplify the model configuration. In the future work, the artificial intelligence techniques, such as neural network (NN), support vector machine (SVM), adaptive neuro-fuzzy inference system (ANFIS), etc, will be employed to develop the learning models to associate the parameters of the proposed model to physical parameters or material properties of the composite joint that facilitates the engineering application in the real condition.

Acknowledgments

The authors would like to appreciate the financial supports provided by National Natural Science Foundation of China (Grant No. 51650110509 and 51678322), and Australian Research Council via Research Hub (IH150100006) for Nanoscience Based Construction Materials Manufacturing (NANOCOMM). Besides, Dr. Rui Li and technical staff of Centre for Infrastructure Engineering at Western Sydney University are greatly thanked for the design and testing of joint specimens.

References

Al Shayokh, M. and Shin, S.Y. (2017), "Bio inspired distributed WSN localization based on chicken swarm optimization", *Wireless Pers. Commun.*, **97**(4), 5691-5706. https://doi.org/10.1007/s11277-017-4803-1

AS 1012.9 (2014), Methods of testing concrete, Method 9: compressive strength tests-concrete, mortar and grout specimens, Standards Australia; Sydney, Australia.

AS 1012.10 (2014), Methods of testing concrete, Method 10: determination of indirect tensile strength of concrete cylinders ('Brazil' or splitting test), Standards Australia; Sydney, Australia.

AS 2327.1 (2003), Composite structures, Part 1: simply supported beams, Standards Australia; Sydney, Australia.

Baber, T.T. and Noori, M.N. (1985), "Random vibration of degrading, pinching systems", *J. Eng. Mech.*, **111**(8), 1010-1026. https://doi.org/10.1061/(ASCE)0733-9399(1985)111:8(1010)

Baber, T.T. and Wen, Y.K. (1981), "Random vibration hysteretic, degrading systems", *ASCE J. Eng. Mech. Div.*, **107**(6), 1069-1087.

BS EN 1993-1-1 (2005), Design of steel structures, Part 1. 1: general rules and rules for buildings, British Standards Institution; London, United Kingdom.

BS EN 1994-1-1 (2006), Design of composite steel and concrete structures, Part 1. 1: general rules and rules for buildings, British Standards Institution; London, United Kingdom.

Chao, S.H. and Loh, C.H. (2009), "A biaxial hysteretic model for a structural system incorporating strength deterioration and pinching phenomena", *Int. J. Nonlin. Mech.*, **44**(7), 745-756. https://doi.org/10.1016/j.ijnonlinmec.2009.04.005

Chen, S., Yang, R., Yang, R., Yang, L., Yang, X., Xu, C., Xu, B., Zhang, H., Lu, Y. and Liu, W. (2016), "A parameter estimation method for nonlinear systems based on improved boundary chicken swarm optimization", *Discrete Dyn. Nat. Soc.*, **2016**, 3795961. http://dx.doi.org/10.1155/2016/3795961

Clough, R.W. and Johnston, S.B. (1966), "Effect of stiffness degradation on earthquake ductility requirements", *Proceedings of the 2nd Japan National Conference on Earthquake Engineering, International Association for Earthquake Engineering*, Tokyo, pp. 227-232.

Das, A., Hirwani, C.K., Panda, S.K., Topal, U. and Dede, T. (2018), "Prediction and analysis of optimal frequency of layered composite structure using higher-order FEM and soft computing techniques", *Steel Compos. Struct., Int. J.*, **29**(6), 749-758. https://doi.org/10.12989/scs.2018.29.6.749

Dowell, R.K., Seible, F. and Wilson, E.L. (1998), "Pivot hysteresis model for reinforced concrete members", *ACI Struct. J.*, **95**(5), 607-617.

Farrokh, M., Dizaji, M.S. and Joghataie, A. (2015), "Modeling hysteretic deteriorating behavior using generalized prandtl neural network", *J. Eng. Mech.*, **141**(8), 04015024. https://doi.org/10.1061/(ASCE)EM.1943-7889.0000925

Foliente, G.C. (1995), "Hysteresis modeling of wood joints and structural systems", *J. Struct. Eng.*, **121**(6), 1013-1022. https://doi.org/10.1061/(ASCE)0733-9445(1995)121:6(1013)

Han, L.-H., Xu, C.-Y. and Tao, Z. (2019), "Performance of concrete filled stainless steel tubular (CFSST) columns and joints: Summary of recent research", *J. Constr. Steel Res.*, **152**, 117-131. https://doi.org/10.1016/j.jcsr.2018.02.038

Ho-Huu, V., Vo-Duy, T., Duong-Gia, D. and Nguyen-Thoi, T. (2018), "An efficient procedure for lightweight optimal design of composite laminated beams", *Steel Compos. Struct., Int. J.*, **27**(3), 297-310. https://doi.org/10.12989/scs.2018.27.3.297

Ibarra, L.F., Medina, R.A. and Krawinkler, H. (2005), "Hysteretic models that incorporate strength and stiffness deterioration", *Earthq. Eng. Struct. D.*, **34**(12), 1489-1511. https://doi.org/10.1002/eqe.495

Li, D., Uy, B., Patel, V. and Aslani, F. (2017a), "Analysis and design of demountable embedded steel column base connections", *Steel Compos. Struct., Int. J.*, **23**(3), 303-315. https://doi.org/10.12989/scs.2017.23.3.303

Li, R., Samali, B., Tao, Z. and Hassan, M.K. (2017b), "Cyclic behaviour of composite joints with reduced beam sections", *Eng. Struct.*, **136**, 329-344.

Li, D., Uy, B., Patel, V. and Aslani, F. (2018a), "Behaviour and design of demountable CFST column-column connections

subjected to compression", *J. Constr. Steel. Res.*, **141**, 262-274. https://doi.org/10.1016/j.jcsr.2017.11.021

Li, D., Wang, J., Uy, B., Aslani, F. and Patel, V. (2018b), "Analysis and design of demountable circular CFST column-base connections", *Steel Compos. Struct., Int. J.*, **28**(5), 559-571. https://doi.org/10.12989/scs.2018.28.5.559

Liu, D., Liu, C., Fu, Q., Li, T., Khan, M.I., Cui, S. and Faiz, M.A. (2018), "Projection pursuit evaluation model of regional surface water environment based on improved chicken swarm optimization algorithm", *Water Resour. Manag.*, **32**(4), 1325-1342. https://doi.org/10.1007/s11269-017-1872-6

Ma, D.-Y., Han, L.-H. and Zhao, X.-L. (2019), "Seismic performance of the concrete-encased CFST column to RC beam joint: Experiment", *J. Constr. Steel. Res.*, **154**, 134-148. https://doi.org/10.1016/j.jcsr.2018.11.030

McCrum, D.P., Simon, J., Grimes, M., Broderick, B.M., Lim, J.B.P. and Wrzesien, A.M. (2019), "Experimental cyclic performance of cold-formed steel bolted moment resisting frames", *Eng. Struct.*, **181**, 1-14. https://doi.org/10.1016/j.engstruct.2018.11.063

Meng, X., Liu, Y., Gao, X. and Zhang, H. (2014), "A new bio-inspired algorithm: Chicken swarm optimization", *Lect. Notes Comput. Sci.*, **8794**, 86-94. https://doi.org/10.1007/978-3-319-11857-4_10

Ning, C., Yu, B. and Li, B. (2016), "Beam-column joint model for nonlinear analysis of non-seismically detailed reinforced concrete frame", *J. Earthq. Eng.*, **20**(3), 476-502. https://doi.org/10.1080/13632469.2015.1104759

Nithyadharan, M. and Kalyanaraman, V. (2013), "Modelling hysteretic behaviour of cold-formed steel wall panels", *Eng. Struct.*, **46**, 643-652. https://doi.org/10.1016/j.engstruct.2012.08.022

Otani, S. and Sozen, M. (1974), "Simulated earthquake tests of R/C frames", *ASCE J. Eng. Mech. Div.*, **100**, 687-701.

Ozcebe, G. and Saatcioglu, M. (1989), "Hysteretic shear model for reinforced concrete members", *J. Struct. Eng.*, **115**(1), 132-148. https://doi.org/10.1061/(ASCE)0733-9445(1989)115:1(132)

Ray, T. and Reinhorn, A.M. (2014), "Enhanced smooth hysteretic model with degrading properties", *J. Struct. Eng.*, **140**(1), 04013028. https://doi.org/10.1061/(ASCE)ST.1943-541X.0000798

Sengupta, P. and Li, B. (2013), "Modified Bouc–Wen model for hysteresis behavior of RC beam–column joints with limited transverse reinforcement", *Eng. Struct.*, **46**, 392-406. https://doi.org/10.1016/j.engstruct.2012.08.003

Sengupta, P. and Li, B. (2014), "Hysteresis behavior of reinforced concrete walls", *J. Struct. Eng.*, **140**(7), 04014030. https://doi.org/10.1061/(ASCE)ST.1943-541X.0000927

Sezen, H. and Chowdhury, T. (2009), "Hysteretic model for reinforced concrete columns including the effect of shear and axial load failure", *J. Struct. Eng.* **135**(2), 139-146. https://doi.org/10.1061/(ASCE)0733-9445(2009)135:2(139)

Sofianos, C.D. and Koumousis, V.K. (2018), "Hysteretic beam element with degrading smooth models", *Arch. Appl. Mech.*, **88**(1-2), 253-269. https://doi.org/10.1007/s00419-017-1263-8

Thai, H.-T. and Uy, B. (2015), "Finite element modelling of blind bolted composite joints", *J. Constr. Steel. Res.*, **112**, 339-353. https://doi.org/10.1016/j.jcsr.2015.05.011

Thai, H.-T. and Uy, B. (2016), "Rotational stiffness and moment resistance of bolted endplate joints with hollow or CFST columns", *J. Constr. Steel. Res.*, **126**, 139-152. https://doi.org/10.1016/j.jcsr.2016.07.005

Varnava, V. and Komodromos, P. (2013), "Assessing the effect of inherent nonlinearities in the analysis and design of a low-rise base isolated steel building", *Earthq. Struct., Int. J.*, **5**(5), 499-526. https://doi.org/10.12989/eas.2013.5.5.499

Veletsos, A.S., Newmark, N.M. and Chelapati, C.V. (1965), "Deformation spectra for elastic and elastoplastic systems subjected to ground shock and earthquake motions", Wellington, New Zealand, January.

Wang, J.F., Han, L.H. and Uy, B. (2009), "Hysteretic behaviour of flush end plate joints to concrete-filled steel tubular columns", *J. Constr. Steel Res.*, **65**(8-9), 1644-1663. https://doi.org/10.1016/j.jcsr.2008.12.008

Wang, P.H., Ou, Y.C. and Chang, K.C. (2017), "A new smooth hysteretic model for ductile flexural-dominated reinforced concrete bridge columns", *Earthq. Eng. Struct. D.*, **46**(14), 2237-2259. https://doi.org/10.1002/eqe.2875

Wang, J., Zhu, H., Uy, B., Patel, V., Aslani, F. and Li, D. (2018), "Moment-rotation relationship of hollow-section beam-to-column steel joints with extended end-plates", *Steel Compos. Struct., Int. J.*, **29**(6), 717-734. https://doi.org/10.12989/scs.2018.29.6.717

Wang, J., Yang, J. and Cheng, L. (2019), "Experimental study of seismic behavior of high-strength RC columns strengthened with CFRP subjected to cyclic loading", *J. Struct. Eng.*, **145**(2), 04018240. https://doi.org/10.1061/(ASCE)ST.1943-541X.0002251

Wen, Y.K. (1976), "Method for random vibration of hysteretic systems", *ASCE J. Eng. Mech. Div.* **102**(2), 249-263.

Wu, D., Xu, S. and Kong, F. (2016), "Convergence analysis and improvement of the chicken swarm optimization algorithm", *IEEE Access*, **4**, 9400-9412. https://doi.org/10.1109/ACCESS.2016.2604738

Yu, B., Ning, C. and Li, B. (2016), "Hysteretic model for shear-critical reinforced concrete columns", *J. Struct. Eng.*, **142**(9), 04016056. https://doi.org/10.1061/(ASCE)ST.1943-541X.0001519

BU